

1
2
3
4
5
6
7
8
9
10
11
12
13
14
15
16
17
18
19
20
21
22
23
24
25
26
27
28
29
30
31
32
33
34

Earthquake Depth-Energy Release: Thermomechanical Implications for Dynamic Plate Theory

Running title: EARTHQUAKE DEPTH-ENERGY RELEASE

Words abstract: 290

Words text: 13552

References: 93

Tables: 6

Figures: 9

R. L. Patton

School of Environmental Sciences

Washington State University

Pullman, WA 99164

rpatton@wsu.edu

35 **Abstract.** Analysis of the global centroid-moment tensor catalog reveals significant regional variations of
36 seismic energy release to 290 km depth. The largest variations, with direction from the baseline indicated
37 using plus and minus signs, and in decreasing order, occur at 14-25 km depths in continental transform (+),
38 oceanic ridge/transform (+), continental rift (+), Himalayan-type (+), island arc-type (-) and Andean-type (-
39) margins. At 25-37 km depths, variations one-fifth the size occur in continental rift (+), island arc-type
40 (+), Andean-type, (-), Himalayan-type (-), oceanic ridge/transform (-), and continental transform (-)
41 margins. Below 37-km depth, variations one-tenth the size occur in Andean-type and Himalayan-type
42 margins to depths of about 260 km. Energy release in island arc-type margins closely tracks the baseline to
43 the maximum depth of earthquakes at 699 km. The maximum depth of earthquakes in Andean-type and
44 Himalayan-type margins is 656 and 492 km, respectively, while in divergent and transform margins it is
45 about 50 km. These variations reflect radial and lateral contrasts in thermomechanical competence,
46 consistent with a shear-dominated non-adiabatic boundary layer some 700-km thick, capped by denser
47 oceanic lithosphere as much as 100 km thick, or lighter continental tectosphere 170 to 260 km thick. Thus,
48 isobaric shearing at fractally-distributed depths likely facilitates toroidal plate rotations while minimizing
49 global energy dissipation. Shear localization in the shallow crust occurs as dislocations at finite angles with
50 respect to the shortening direction, with a 30 degree angle being the most likely. Consequently, relatively
51 low-angle ($\sim 30^\circ$) reverse faults, steep ($\sim 60^\circ$) normal faults, and triple junctions with orthogonal or
52 hexagonal symmetry are likely to form in regions of crustal shortening, extension, and transverse motion,
53 respectively. Thermomechanical theory also predicts adiabatic conditions in the mantle below about 1000-
54 km depth, consistent with observed variations in bulk sound speed.

55 **1.0 Introduction**

56 A century ago, the solid mechanical properties of rocks factored highly in the development of the isostatic
57 hypothesis, which holds that Earth's outer layers, the crust and lithosphere, are strong and capable of
58 supporting loads for geological time periods (Watts, 2001). Vertical motions of the lithosphere, in response
59 to progressive sedimentary loading, volcano construction, and the advance of ice sheets, are accommodated
60 by deformation of a subjacent weak asthenosphere (Barrell, 1914). Subsequent removal of loads, due to
61 erosion or ablation, results in the rebound of formerly depressed areas. Thus a dynamic equilibrium
62 between Earth's shape, topography, and external gravity field is maintained.

63
64 In principle, the relative horizontal motions of continents suggested by Wegener (1966) are consistent with
65 the presence of the asthenosphere. Still, the mechanism he proposed, continental 'rafts' plowing
66 undeformed through oceanic crustal 'seas' under the influence of centrifugal forces, is at odds with the
67 known contrast between stronger mafic oceanic crustal rocks and weaker felsic continental ones.

68 Consequently, wide acceptance of continental drift had to await the development of the sea floor spreading
69 hypothesis (Dietz, 1961; Hess, 1962), and recognition of Benioff (1954) zones as down going extensions of
70 oceanic lithosphere. Thus, the continents appear to be embedded within blocks of mobile lithosphere, the
71 horizontal motion of which is decoupled from the deeper mantle by the asthenosphere, and accommodated
72 by its progressive creation and destruction at oceanic ridges and trenches, respectively (Isacks et al., 1968).
73 Lithosphere is neither created nor destroyed at transform faults, where the relative motion of adjacent
74 blocks is parallel to the fault (Wilson, 1965).

75
76 In the late 1960's, the kinematic theory of plate tectonics (Le Pichon, 1968; McKenzie and Morgan, 1969;
77 McKenzie and Parker, 1967; Morgan, 1968; Wilson, 1965) successfully explained global map patterns of
78 earthquake foci and first motions (Isacks et al., 1968), and systematic variations of sea floor age across
79 active oceanic ridges (Vine and Matthews, 1963), via the relative horizontal motion of rigid spherical caps.
80 Attempts to reconcile this new theory with observed patterns in continental geology followed soon after
81 (Atwater, 1970; Dewey and Bird, 1970), but the rigidity assumption has never sat well with the overall
82 width of, and diffuse nature of deformation in, mountain belts. Other limitations of plate theory include its

83 inability to account for known differences in the density and strength of crustal rocks between oceans and
84 continents, and the various thickness estimates for the crust (Rudnick and Gao, 2003) and oceanic
85 lithosphere (Parsons and Sclater, 1977), as well as stable cratons and shields (Artemieva, 2009; Artemieva
86 et al., 2004; Artemieva and Mooney, 2001). Moreover, it does not predict the existence of seismicity, but
87 rather uses it to define the boundaries of, and relative motions between, its plate-like blocks. These
88 boundaries apparently act as long-lived zones of weakness in the global plate system. The dynamic basis
89 for plate theory and its relation to motions in the deeper mantle remain poorly understood (Bercovici et al.,
90 2000; McKenzie, 1969; Tackley, 2000).

91

92 In order to simulate horizontal (toroidal) rotations of plate-like blocks many variations of the standard Earth
93 model (Bercovici et al., 2000) incorporate *ad hoc* mechanisms for shear localization. However, because
94 these mechanisms are based on temperature-dependent variations in viscosity, and ideal viscous materials
95 do not manifest shear bands or dislocations, they cannot account for seismicity. This also holds for power
96 law viscous, i.e. Reiner-Rivlin, materials. Although these materials can produce shear bands for exponents
97 $2 \leq n < \infty$, they cannot simultaneously propagate shear waves, and hence are rheological fluids (Patton and
98 Watkinson, 2010). Therefore, a major stumbling block to further progress on the dynamic plate problem is
99 not a lack of data, but rather a deficiency in applied rheological theory.

100

101 Since the mid-1960's, space-based geodesy has provided global gravity and topography datasets with ever
102 increasing quality and resolution. Today, the tracking of satellite orbits constrains the low-frequency
103 harmonics of Earth's external gravity field, with half-wavelengths ($\lambda_{l/2}$) greater than about 200 km
104 (spherical harmonic degrees $l < 100$). Analysis of these data, combined with gravimetric survey and global
105 topography data (Amante and Eakins, 2009), show that Earth's gravity and topography are correlated ($r =$
106 $0.6-0.7$) for $\lambda_{l/2} < 1000$ ($l > 20$) (Wieczorek, 2007), consistent with isostasy at a regional level (Watts,
107 2001). It is therefore common to hear tectonic specialists talking about the effective elastic thickness of the
108 crust and lithosphere. The gravity-topography correlation diminishes rapidly for $l \leq 20$, which implies that
109 vertical (poloidal) motions in the mantle actively support the longest wavelength gravity and geoid
110 anomalies (McKenzie, 1967).

111

112 An outstanding question for dynamic Earth models, and the standard model in particular, is whether long-
 113 wavelength gravity anomalies can be associated unequivocally with sub-lithospheric mantle convection
 114 (Kaula, 1972; Steinberger et al., 2010) and so-called dynamic topography (Hager, 1984; Panasyuk and
 115 Hager, 2000). Here I show that key features of Earth's gravity-topography correlation and admittance can
 116 be explained using a thermomechanical boundary layer hypothesis, which constrains the possible range of
 117 wavelengths associated with standard convection to $\lambda_{1/2} > 2500 \text{ km}$ ($l < 8$). This limit is far larger than the
 118 $\lambda_{1/2} > 650 \text{ km}$ ($l < 3l$) one identified by Steinberger *et al* (2010) based on empirical 'downward
 119 continuation' of gravity spectra and crustal thickness modeling, and wholly consistent with the scale of
 120 robust heterogeneities revealed by seismic tomography (Dziewonski et al., 1977; Dziewonski and
 121 Woodward, 1992; Gu et al., 2001).

122

123 Establishment of the Global Positioning System (GPS) in the early 1990's makes it possible to account for
 124 ever longer-period neotectonic deformations. These new datasets have been used recently to estimate
 125 density-normalized rates of mechanical energy dissipation χ [m^2s^{-1}] in plate boundary zones, which fall in
 126 the range $4.2 \leq -\log \chi \leq 5.2$, and also in intraplate regions, which fall in the range $5.3 \leq -\log \chi \leq 7.0$ (Patton
 127 and Watkinson, 2010). As shown later in the paper, similar estimates of χ for spontaneous-failures in load
 128 hold experiments on the Mt. Scott granite (Katz and Reches, 2002, 2004) fall in the range $2.3 \leq -\log \chi \leq$
 129 5.6 . The overlap in these estimates suggests that joint analysis of neotectonic survey and rock mechanics
 130 data could constrain natural rates of energy dissipation in the broad deforming plate boundary regions,
 131 which have been so problematic for the kinematic theory.

132

133 Furthermore, by comparing these mechanical dissipation estimates to measured rates of thermal energy
 134 dissipation κ [m^2s^{-1}] in silicates, e.g. $5.9 \leq -\log \kappa \leq 6.3$ (Clauser and Huenges, 1995; Vosteen and
 135 Schellschmidt, 2003), it is possible to define the thermomechanical competence of solid earth materials by
 136 the ratio κ/χ . Note, for values of $\kappa/\chi < 1$, the rate of mechanical dissipation is higher than thermal
 137 dissipation, so that as a material deforms it carries its heat along. Conversely, values of $\kappa/\chi > 1$ imply that
 138 the rate of thermal dissipation is higher than mechanical dissipation, so that heat will be conducted readily

139 through a material while it deforms only slightly. This, in a nutshell, is the thermomechanical rigidity
 140 hypothesis (Patton and Watkinson, 2010), which is used here to interpret observed variations in seismic
 141 energy release. This definition of rigidity retains its practical meaning as a resistance to shape changes,
 142 while shedding the highly idealized kinematic connotation of no internal deformation under loading.

143

144 Mechanical properties also factor highly in seismological models for wave propagation, and are critical for
 145 inferring first-order planetary structure, like the existence and nature of the mantle and core. As is well-
 146 known, the lack of shear wave propagation through the outer core is consistent with its existence in the
 147 liquid phase, while the propagation of shear waves in the mantle and inner core is consistent with their
 148 existence in the solid phase. Additionally, the attenuation of surface waves in the shallow asthenosphere,
 149 coincident with the low velocity zone, is consistent with the presence of a partial melt phase (Presnall and
 150 Gudfinnsson, 2008), although solid-state anelasticity also plays a role (Jackson et al., 2005; Karato, 1993).

151

152 Defining thermomechanical competence by the ratio κ/χ has the advantage of being testable, and free of the
 153 confounding aspects of the effective elastic thickness estimated in regional isostasy studies (Watts, 2001).
 154 For example, if the entire mantle propagates shear waves and is therefore an elastic solid, how can it make
 155 sense to further define plate-like blocks by their effective elastic thickness? Granted, the seismologic and
 156 isostatic models serve different purposes, and hence their use of the term ‘elastic’ need not be consistent.
 157 Nevertheless, a consistent definition of material competence is required for any dynamic plate theory, and I
 158 shall use thermomechanical competence throughout.

159

160 Adams and Williamson (1923), and later Birch (1952), used the relation

$$161 \quad K_s / \rho = V_p^2 - (4/3)V_s^2 = V_\phi^2 \quad (1)$$

162 where K_s is adiabatic bulk incompressibility and ρ is density, to study the thermodynamics of the mantle
 163 based on observed radial variations in compressional V_p , shear V_s , and bulk sound V_ϕ wave speeds.

164 Birch inferred that the mantle below about 900-km depth was chemically homogeneous and adiabatic,
 165 while between 200- and 900-km depths it was not. Furthermore, he was among the first to suggest the

EARTHQUAKE DEPTH-ENERGY RELEASE

166 importance of mineral phase changes in the upper transitional zone. Seismological data collected since the
167 1950's have done nothing but reinforce Birch's insights (Dziewonski and Anderson, 1981). Clearly, there
168 is something unusual about the upper mantle that must be understood thermodynamically.

169

170 Proponents of the standard Earth model often point to the apparent adiabaticity of the lower mantle as
171 evidence for its vigorous convection. Although an adiabatic gradient can be maintained by the efficient
172 mixing of material in viscous convection cells at high Rayleigh number (Turcotte and Oxburgh, 1967),
173 adiabaticity also prevails in the lower reaches of a solid thermomechanical mantle, whether it is convecting
174 or not. Furthermore, because the thermal expansivity of such mantle is inversely proportional to
175 temperature, any convection process in the lower, hotter, mantle would likely be rather sluggish compared
176 to that in the upper mantle. These conclusions, based on the statistical thermodynamics of non-linear
177 elastic solids, are consistent with those based on the compressibility and rigidity of likely lower mantle
178 mineral species (Anderson, 1989, 2007).

179

180 In summary, any dynamic plate theory should predict the plate-like nature of Earth's outer shell, provide
181 self-consistent mechanisms for its toroidal motion and spontaneous localization of shear, and explain the
182 observed spectral correlation and admittance of Earth's topography and gravity. In doing so, the nature of
183 coupling between the plate-like blocks at the surface and poloidal motions in the mantle should be made
184 clear. Proponents of the standard Earth model emphasize the insignificance of crustal and lithospheric
185 strength on the length and time scales of geodynamics, and point to estimates of mantle viscosity based on
186 glacial-isostatic rebound as evidence in favor of their view. This stance is necessary, only because the
187 rheological theory upon which the standard model is based does not account for material strength or shear
188 localization.

189

190 Here, I adopt the complimentary stance, and ask what are the length and time scales over which the force of
191 gravity acts within the body of a solid thermomechanical planet. In deriving the dynamic rescaling theorem
192 for deforming differential grade-2 (DG-2) solids (Patton and Watkinson, 2010), I have come to realize that
193 rock strength always matters, not only for plate theory but also for the entire mantle. Thus, the

194 confounding semantics of rock ‘viscosity’ are moot, because a clear theoretical distinction exists between
195 the deformation of thermomechanical solids on the one hand, and thermoviscous fluids on the other.
196 Consequently, the density-normalized rates of mechanical energy dissipation measured in rock mechanics
197 experiments can be applied immediately to the dynamic plate problem, regardless of whether they are
198 termed kinematic viscosities or mechanical diffusivities. Henceforth, I shall adopt the latter term, in an
199 effort to discourage further semantic confusion.

200

201 This study interprets earthquake depth-energy release patterns for tectonically regionalized data from the
202 global centroid-moment tensor (CMT) catalog (Ekstrom and Nettles, 2011), using insights from the
203 thermomechanical theory of non-linear elastic DG-2 materials (Patton, 1997; Patton et al., 2000; Patton and
204 Watkinson, 2005; Patton and Watkinson, 2010, in review). These materials exhibit both distributed
205 harmonic and localized shear band modes of deformation as a function of κ/χ . Harmonic modes alone are
206 possible for $0 < \kappa/\chi < 1/2$, while both harmonic and shear band modes are possible for $\kappa/\chi > 1/2$. This
207 transition occurs on a domain of thermomechanical competence lower than that associated with rigidity.
208 Consequently, theory predicts that even rigid materials can suffer irreversible shear band deformation.
209 Because shear localization liberates strain energy and increases entropy, it is reasonably identified with
210 earthquake faulting and damage. The spontaneous nature of this transition therefore offers a unique
211 opportunity to incorporate global seismicity into dynamic plate theory in a self-consistent manner.

212

213 Section 2.0 of the paper examines the map, magnitude, and depth distribution of seismicity as sampled by
214 the CMT catalog, and explains the method and rationale for computing earthquake depth-energy release
215 curves. It compares and contrasts depth variations in this signal using a six-fold classification of tectonic
216 margins. This section provides some background on the CMT inversion process, as compared to typical
217 earthquake location methods, so that the relevance of CMTs to dynamic plate theory is clear.

218

219 Section 3.0 outlines a statistical thermodynamic theory for strained inhomogeneous elastic and self-
220 gravitating matter configurations (Lavenda, 1995), which place severe constraints on the slope and shape of
221 the energy density as a function of entropy and length. This theory makes specific predictions about

EARTHQUAKE DEPTH-ENERGY RELEASE

222 temperature and pressure variations and the temperature dependence of thermal expansivity in these
223 materials. Alone, these findings are consistent with expected variations of pressure and temperature in
224 terrestrial planets, but offer no insight into observed variations of seismic energy release with depth in the
225 Earth. Consequently, they provide essential foil for the thermomechanics of shear localization in DG-2
226 materials.

227

228 Section 4.0 outlines a statistical thermomechanical theory for DG-2 materials. It builds upon the
229 consistency of the slope and shape of the distributed energy threshold (ψ^D) for DG-2 materials with the
230 constraints derived in Section 3, and its interpretation as an elastic strain-energy function (Patton and
231 Watkinson, 2005), to place earlier published work on these ideal materials in a very general and
232 geologically useful context. Domains of κ/χ for which harmonic and shear band modes of deformation are
233 possible are deduced using incipient modes analysis.

234

235 Section 5.0 applies thermomechanical theory to the interpretation and correlation of published data from
236 rock mechanics experiments on the Mt. Scott Granite (2002, 2004). Not only does the localization curve
237 (ψ^L) on the lower-competence harmonic domain neatly divide the sample population into macroscopically
238 failed and un-failed groups, but it also correlates with post-loading observations of microscopic crack and
239 macroscopic shear angles on the mixed harmonic-shear band domain at higher competence. The dynamic
240 rescaling of lengths during sample failure is likely (Patton and Watkinson, 2010), given that the pre- and
241 post-failure observations span the non-convex portion of the localization curve (Hobbs et al., 2011).

242 Dynamic shear failure in these rock samples therefore minimizes energy dissipation in the combined
243 sample-load frame system. Data from three samples suffering spontaneous shear localization are used to
244 estimate mechanical diffusivity χ .

245

246 Section 6.0 expands upon the isobaric shearing hypothesis (Patton and Watkinson, 2010) and its utility for
247 the interpretation of Earth structure. Predicted depths to these theoretical shears, empirically calibrated via
248 least-squares minimization of ThERM to PREM (Patton, 2001; Patton and Watkinson, 2009, 2010), are
249 consistent with observed variations of earthquake depth-energy release. Furthermore, their fractal depth

250 distribution suggests that Earth's dynamic plate system globally minimizes energy dissipation. The
251 structure of the lithosphere and asthenosphere, together, comprise a thermomechanical boundary layer
252 adjacent of the surface of the planet.

253

254 Section 7.0 discusses the implications of these findings for the interpretation of rock mechanics data,
255 pressure-temperature-time data from structural and metamorphic studies in orogens, likely source depths
256 for common intrusive and extrusive rocks, the lateral variability of seismic wave speeds in the upper mantle
257 and crust, and the spectral correlation and admittance of Earth's gravity and topography.

258

259 Section 8.0 concludes the paper with the notion that coupled toroidal-poloidal motions of Earth's plate-like
260 blocks represent a top-down mode of convection peculiar to solid thermomechanical planets. Given the
261 generality of the theory upon which these conclusions rest, and its remarkable correlation with datasets
262 from a wide range of fields, it is likely that the absence of plate-like convection on other terrestrial planets
263 can be attributed to the small size of the sample population, as well as the lack of liquid water on the known
264 examples. Water and other volatile species tend to weaken, i.e. increase the mechanical diffusivity of,
265 common rocks and minerals.

266

267 **2.0 Earthquake depth-energy release**

268 2.1 Locating earthquakes

269 Since about 1970, earthquake hypocenters have been routinely and rapidly located using telemetric
270 monitoring networks established by the United States Geological Survey, and many other agencies, for the
271 purpose of mitigating earthquake hazards. These networks typically use body wave first motions to
272 triangulate event locations within radially-symmetric elastic Earth models (Kennett and Engdahl, 1991),
273 although for the past 15 years or so depth phases also have been used (Engdahl et al., 1998). Body waves
274 propagate freely through solids with lateral extents much greater than the wavelength of the waves
275 themselves. They are highly sensitive to variations in density and elastic moduli at the scale of about one-
276 half their wavelength. Consequently, the average error for hypocenter depth in standard catalogs, like the

EARTHQUAKE DEPTH-ENERGY RELEASE

277 Preliminary Determination of Epicenters, is about 14 km (Kennett and Engdahl, 1991). Hypocenter depths
278 for 20646 earthquakes are shown in Figure 1a.

279

280 By the time of the 1960 May 22 M_w 9.5 Chile earthquake, which started the planet ringing like a bell,
281 instrumentation had been developed that allowed the first precise studies of Earth's free oscillations. These
282 so called normal modes have periods as long as 54 minutes, and their observation spawned a whole new
283 area of seismological research. Subsequent theoretical developments showed that the precise location of
284 earthquakes, and their detailed dislocation characteristics, could be determined within the body of an Earth
285 model by summing these normal modes (Dziewonski et al., 1981; Dziewonski and Woodhouse, 1983;
286 Ekstrom et al., 2012). This CMT method accounts for long-period energy that is not possible via first
287 motions of body waves alone, and does not require a radially-symmetric reference model. Furthermore, it
288 is insensitive to lateral heterogeneity at scales less than half the wavelength of a given normal mode (Luh,
289 1975; Madariaga, 1972).

290

291 Since the early 1980's, recordings of well-observed earthquakes have been routinely inverted for their
292 CMT characteristics via normal modes summation (Dziewonski et al., 1981; Dziewonski and Woodhouse,
293 1983; Ekstrom et al., 2012). In this process the triangulated hypocenter is taken as the initial estimated
294 location of a shear dislocation, which is then refined by accounting for the energy contained in the gravest
295 and progressively higher frequency modes. Centroid depths for 20646 of these are shown in Figure 1b.
296 The global CMT catalog, begun by Adam Dziewonski and co-workers at Harvard, is now maintained under
297 the CMT project (Ekstrom and Nettles, 2011) at Lamont-Doherty Earth Observatory.

298

299 CMT inversion initially took into account long-period body waves (Dziewonski et al., 1981), with peak
300 spectral energy between about 16.7 to 20 mHz, and Earth's free oscillations with frequencies lower than 7.4
301 mHz (Dziewonski and Woodhouse, 1983), the so-called 'mantle waves'. However, since 2004 normal
302 modes with frequencies in the intermediate 7.4 to 16.7 mHz range, which are strongly affected by lateral
303 Earth structure (Luh, 1975; Madariaga, 1972), also have been used in routine inversions (Ekstrom et al.,

304 2012). As a result the practical lower limit on event magnitude, initially $M_w > 5.5$ and associated with a
305 frequency cut-off above about 22 mHz, has decreased to about $M_w > 5.0$.

306

307 Reference models used by the CMT project include the radially-symmetric PREM (Dziewonski and
308 Anderson, 1981) and shear attenuation model QL6 (Durek and Ekstrom, 1996), and a mantle heterogeneity
309 model called SH8U4L8 (Dziewonski and Woodward, 1992). The latter model accounts for lateral
310 variations in shear wave speeds at half-wavelengths as small as about 2500 km ($l \leq 8$), in four layers of the
311 upper mantle, and eight layers of the lower mantle. Lateral variations of this scale represent the most
312 robust deviations from spherical symmetry, as imaged by global tomographic models (Dziewonski et al.,
313 1977; Gu et al., 2001). Furthermore, the majority of shear attenuation occurs in the upper mantle, above
314 about 670-km depth (Durek and Ekstrom, 1996; Romanowicz, 1994; Romanowicz, 1995; Widmer et al.,
315 1991).

316

317 2.2 Effects of CMT relocation

318 The CMT catalog, downloaded from www.globalcmt.org, includes data for 30872 earthquakes recorded
319 during the period January 1976 through December 2010. Of these only 20646 were relocated by the CMT
320 procedure (Ekstrom and Nettles, 2011), and therefore have quantitative error estimates. The remaining
321 events either had their focal depths fixed by an analyst, or constrained by an inversion of short-period data.
322 The consistent algorithmic treatment of the 20646 relocated events, and the fact that CMTs estimate the
323 total work done by a seismic dislocation, make them ideal for the tectonic analysis presented here.

324

325 Mean standard errors for CMT latitude, longitude, and depth are 0.042° , 0.047° , and 2.82 km, respectively.
326 The depth error estimate defines the minimum thickness of a filter used to smooth the earthquake depth-
327 energy release curves presented here. A filter smaller than this tends to display more noise than a larger
328 one, while larger filters discard potentially interpretable depth signal in the dataset, at least at typical crustal
329 depths. Depth-energy release curves shown here were smoothed using either 3-km or 10-km filters.

330

EARTHQUAKE DEPTH-ENERGY RELEASE

331 Initial hypocenters and relocated centroids are distributed differently with both magnitude (Table 1) and
332 depth (Table 2). Centroids generally have higher moment magnitudes than their associated hypocenters,
333 consistent with the fact that longer-period energy is accounted for in their estimation. All 20646 relocated
334 events appearing in the catalog are accounted for in the moment release studies presented here. Most of the
335 seismic signal is present in the $M_w=5-6$ band, with significant signal also in the $M_w=4-5$ and $M_w=6-7$ bands.
336 The depth distributions of hypocenters and centroids are significantly different in the crust, above about 37-
337 km depth. Small differences in map locations exist as well, but these do not significantly alter the global
338 map pattern of seismicity, and are not discussed further.

339
340 Figure 1 shows differences in the depth distribution of earthquake hypocenters and centroids, using a color-
341 key linearly distributed, piecewise, between 0- and 800-km depths (Table 2). Subtle differences in color
342 values therefore reflect real depth differences between events. The depth intervals were chosen consistent
343 with ThERM modes H4, L1, L2, L4, M1, M2, and M4 (Patton and Watkinson, 2010) (Table 3).

344
345 In the upper crust, 0-14.4 km depth, there are about three times as many hypocenters as there are centroids,
346 and the color palette ranges from red to orange (Table 2). The map distribution of events is similar for both
347 hypocenters and centroids. Events commonly occur at oceanic ridges, oceanic trenches, and the Alpine-
348 Himalayan belt. The centroids are distinctly deeper than their corresponding hypocenters.

349
350 In the middle crust, 14.4-25 km depth, the number of hypocenters is only about one-fifth that of centroids
351 and the color palette ranges from orange to yellow. The map distributions of hypocenters and centroids
352 also show significant differences. While hypocenters are common at all oceanic trenches and along the
353 Alpine-Himalayan belt, they only rarely appear at oceanic ridges. Centroids, in addition to occurring at
354 oceanic trenches and the Alpine-Himalayan belt, are common at oceanic ridges and also major transform
355 boundaries, like the San Andreas-Queen Charlotte-Fairweather fault system.

356
357 In the lower crust, 25-37 km depth, hypocenters outnumber centroids by about 1.5 times, and the color
358 palette ranges from yellow to green. Oceanic trenches are well-populated by both hypocenters and

359 centroids, as is the Alpine-Himalayan belt. Rare intraplate events of both types also appear. Interestingly,
360 centroids also sparsely populate oceanic ridges, but primarily at the shallower (yellow) end of the range.

361

362 In the lithosphere, 37-99.5 km depth, the number of hypocenters and centroids is comparable, and the color
363 palette ranges from green to blue. Hypocenters and centroids are absent at all oceanic ridges and active
364 transform boundaries, but commonly populate all oceanic trenches as well as the Alpine-Himalayan belt.

365 Distinct 'knots' of events appear beneath the Carpathians and the Hindu Kush, with rare events in East
366 Africa-Madagascar. The map distributions of hypocenters and centroids are similar in most respects.

367

368 The number of hypocenters and centroids in subducting slabs transiting the upper tectosphere, 99.5-172 km
369 depth, is comparable, and the color palette ranges from blue to purple. As in the preceding depth interval,
370 the map distributions of events are very similar. Both hypocenters and centroids are well-represented at all
371 oceanic trenches, but also sparsely populate the Alpine-Himalayan belt. The Carpathian and Hindu Kush
372 'knots' persist to these depths as well.

373

374 The number of hypocenters and centroids in subducting slabs transiting the lower tectosphere, 172-255 km
375 depth, is comparable, and the color palette ranges from purple to pink. The maps again are very similar,
376 with hypocenters and centroids common at all oceanic trenches. The Hindu Hush 'knot' persists to these
377 depths as well, but the Carpathian one is absent. Some events also appear beneath the Aegean and southern
378 Italy.

379

380 The number of hypocenters and centroids in subducting slabs transiting the asthenosphere, 255-690 km
381 depth, is comparable, and the color palette ranges from pink to white. Again their map distributions are
382 very similar. Hypocenters and centroids are associated almost exclusively with active subduction margins,
383 e.g. Andes, Tonga-Lau, Malaysia, Indonesia, Japan, Aleutians, South Georgia and Sandwich Islands,
384 except for a few events in the western Alpine Belt, particularly beneath southern Spain and Italy. The
385 Hindu Kush 'knot' appears pink (shallow) in this depth range, consistent with the base of the tectosphere.

386

387 There are only a handful of events in the mesosphere, where the color palette is uniformly black. These
388 events lie only a few kilometers below 690-km depth. Most appear at the Tonga trench, but a few centroids
389 also lie between Japan and Kamchatka.

390

391 In summary, the depth distribution of earthquakes at various plate margins appears to be more consistent
392 for centroids than it does for hypocenters. Thus, while the latter distribution could be interpreted as
393 indicating significant differences in thickness and mechanical properties between oceanic and continental
394 lithosphere, the former distribution suggests the opposite. In both cases, however, the distribution of
395 earthquakes at convergent margins is distinct from that at divergent and transform margins. It is likely that
396 some of the apparent difference between continents and ocean basins is due to the fact that travel-time
397 models are optimized for continents (Kennett and Engdahl, 1991), where the majority of seismic receivers
398 are located. Nevertheless, there are good rock-mechanical reasons to believe that significant differences in
399 the mechanical properties of continents and the ocean basins exist. Therefore, a detailed study of
400 earthquake depth-energy release from tectonically regionalized data might help quantify the nature of these
401 differences.

402

403 2.3 Regional variations

404 Given differences in the depth distribution of earthquakes, noted above, and their apparent correlation with
405 tectonics, it is natural to consider regional subsets of the CMT catalog. These subsets (Figure 2) over
406 sample the CMT catalog by about 0.8% (Table 4). This is due to the expedient method used to select event
407 subsets, particularly at convergent margins where data density is high. It is unlikely, however, that this
408 small discrepancy has any real impact on the conclusions of this report. A more in-depth analysis of these
409 data, including detailed consideration of CMT dislocation characteristics, is in progress.

410

411 Earthquake depth-energy release curves $\Sigma M_w(z;t)$ present the sum of moment magnitudes M_w for
412 earthquakes, filtered for depth z using a boxcar of selected thickness t , at every kilometer from the surface
413 to about 700-km depth. They are an elaboration upon similar curves presented by Frohlich (1989) in his
414 review of deep-focus earthquakes. In early work with the CMT catalog, filter thicknesses of 1, 3, 5, 7, 9,

415 and 11 km, were used, but did not significantly change the depth patterns shown here. The primary effect
416 of filter thickness, apart from curve smoothing, is to change the magnitude of these sums. Consequently,
417 most curves presented here are computed using a 3-km filter, which matches the mean standard depth error
418 of CMTs. This seems to provide adequate smoothing without discarding potential signal. Because moment
419 magnitude is related to scalar seismic moment M_0 [dyne-cm] by the formula $M_w = (2/3)\log_{10}(M_0) - 10.7$ (Aki
420 and Richards, 2002), these curves serve as simple dimensionless proxies for seismic energy release with
421 depth in the planet. How this prevalent, stochastic, and highly localized mode of energy dissipation might
422 be related to energy dissipation in the larger geotectonic system is of primary interest in studying these
423 plots.

424

425 As discussed earlier, well-observed earthquakes with $M_w > 5.0$ are relocated routinely as part of the CMT
426 inversion procedure, using the associated hypocenters as initial estimates. Observed differences between
427 hypocenter and centroid depth-energy release curves can, in part, be understood in this manner. However,
428 the depth-energy release pattern for hypocenters (Figure 3a) is the same for all six tectonic subsets of the
429 earthquakes studied here, as well as for the entire dataset. This is somewhat artificial, and probably reflects
430 optimizations in the quick location algorithms used for event hazard monitoring. On the other hand, the
431 depth-energy release curves for centroids have a more natural appearance (Figure 3b), and reveal
432 interpretable depth structure which apparently depends on the nature of tectonic margins.

433

434 The amplitude of these depth-energy release curves is proportional to the number of events in the given
435 data subset. Consequently, a normalization scheme is needed to enhance possible variations in the depth
436 signal they contain. Given the strong correlation of summed moment magnitude with the number of
437 earthquakes in each subset (Table 4), an expedient normalization scheme is to simply divide $\Sigma M_w(z;t)$ by
438 the number of events N in the subset. Event-normalized earthquake depth-energy release curves
439 $\Sigma M_w(z;t)/N$ reveal significant differences between divergent and transform margins on the one hand and
440 convergent margins on the other. In both panels of Figure 4, the depth-release curve for the entire set of
441 relocated CMTs (black dashed, Table 4) serves as a baseline for these regional comparisons.

442

443 *2.3.1 Divergent and transform margins*

444 The three colored curves shown in Figure 4a correspond to event populations occurring at divergent and
445 transform margins, as plotted in Figure 2a, c, e. There is relatively little energy release associated with the
446 brittle upper crust. In the middle crust, from 14-25 km depths, the most seismic energy is dissipated at
447 continental transforms and oceanic ridges, while the least is dissipated at continental rifts. At all three
448 boundary types, the energy dissipation per event is greater than the global CMT baseline. It is possible that
449 the greater dissipation of energy at continental transforms, compared to the oceanic crust, is due to the
450 lesser Coulomb strength of typical felsic lithologies found there, when compared to mafic ones.

451

452 In the lower crust, from 25-37 km depths, the most seismic energy is dissipated at continental rifts, at a per-
453 event rate higher than the global baseline. In contrast, seismic energy dissipation at oceanic ridges and
454 continental transforms are both significantly below the global baseline, with the least dissipation occurring
455 at continental transforms. This pattern is consistent with the observation that continental crust generally is
456 thicker than ocean crust, and suggests aseismic creep in the lower crust of continental transforms. The
457 similar amounts of energy dissipation in oceanic and continental crust at extensional margins, combined
458 with their differences in thickness, again suggest that oceanic crustal rocks are stronger than continental
459 rocks.

460

461 Below 37-km depth, all three boundaries dissipate less energy than the global per-event baseline, with the
462 most dissipation occurring in continental rifts, and the least in oceanic ridges. Below about 50-km depth,
463 the depth-energy release curves disappear altogether (Table 4). Coincidentally, these depths correspond to
464 a range of pressures thought to be important for the extraction of mid-ocean ridge basalts (MORB)
465 (Presnall and Gudfinnsson, 2008). Perhaps the fact that basalt volcanism is common at oceanic ridges and
466 continental rifts (e.g. East Africa), and not at continental transforms, reflects decompression melting in the
467 mantle at divergent margins.

468

469 *2.3.2 Convergent margins*

470 The three colored curves shown in Figure 4b correspond to event populations occurring at convergent
471 margins, as shown in Figure 2b, d, f. Again, there is relatively little energy release associated with the
472 brittle upper crust. In the middle crust, from 14-25 km depths, the most seismic energy is dissipated at
473 Himalayan-type margins, and at a per-event rate higher than the global CMT baseline. In contrast, the
474 dissipation occurring at island arc-type and Andean-type margins is below the per-event baseline, with the
475 least dissipation occurring at Andean-type margins. This might reflect the juxtaposition of generally
476 thicker and weaker continental crust on both sides of Himalayan-type margins, when compared to the other
477 two margins types.

478

479 In the lower crust, from 25-37 km depths, the most seismic energy is dissipated at island arc-type margins,
480 but at rates only slightly greater than the global per-event baseline. Seismic energy dissipation at Andean-
481 type and Himalayan-type margins is below the global baseline, and while the Andean-type release curve
482 closely parallels the baseline, the Himalayan-type curve deviates substantially.

483

484 Below 37-km depth, seismic energy dissipation in Himalayan-type margins is noticeably less than the
485 global baseline to about 75-km depth. Earthquake depth-energy release curves for convergent margins
486 persist to depths of 492 km at Himalayan-type margins, 656 km at Andean-type margins, and 699 km at
487 island arc-type margins (Table 4). The apparent contrast between convergent and divergent/transform
488 margins, earlier discerned from the seismicity maps, is clearly reflected in these depth variations.

489

490 *2.3.3 Variations throughout the asthenosphere*

491 Given the great depth to which seismic activity occurs at convergent margins, it makes sense to examine
492 deviations from the global baseline throughout the asthenosphere. Again, the depth-release curve for the
493 entire set of relocated CMTs (black dashed, Table 4) serves as a baseline for these regional comparisons.
494 Figure 5 shows event-normalized release curves for the three convergent margin types, filtered using a 10-
495 km boxcar. Relatively large deviations from the global baseline are apparent, particularly at depths less
496 than about 260 km.

497

EARTHQUAKE DEPTH-ENERGY RELEASE

498 In the lithosphere, from 37-100 km depths, seismic energy dissipation at Himalayan-type margins is less
499 than the baseline to about 75-km depth, as noted earlier, while that at Andean-type and island arc-type
500 margins closely parallel the baseline. This might reflect the fact that subduction of oceanic lithosphere is
501 ongoing at the two latter margins, but has ceased at the former.

502

503 In the upper tectosphere, from 100-175 km depths, the greatest energy dissipation occurs at Andean-type
504 margins, and at rates higher than the global baseline. Through this range, energy dissipation at Himalayan-
505 type and island arc-type margins closely tracks the global baseline, except at about 160-180 km depth,
506 where dissipation in the Himalayan-type margins falls off. Coincidentally, these depths correspond to the
507 range of pressures for which peridotite xenoliths in kimberlites show distinct planar tectonite fabrics (Boyd,
508 1973; James et al., 2004). Perhaps this reflects localized weakening of the mantle at these depths,
509 consistent with isobaric shearing at mode M1 of ThERM (Patton and Watkinson, 2010) (Table 3).

510

511 In the lower tectosphere, from 175-260 km depths, seismic energy dissipation at Himalayan-type and
512 Andean-type margins noticeably differ from the global baseline, while that at island arc-type margins
513 closely tracks the baseline. This is consistent with the presence of continental tectosphere (Jordan, 1975) at
514 the former two margin types, and its absence at island arc margins.

515

516 In the asthenosphere, from about 500-650 km depths, the rate of seismic energy dissipation increases. This
517 is a depth range where mineral phase transformations are thought to be likely (Birch, 1952; Ringwood,
518 1991), and it is possible that these earthquakes represent a phase-transformation ‘anti-crack’ population
519 (Green, 2005), although there are other hypotheses (Frohlich, 1989). Seismic energy dissipation tails off
520 substantially at about 660-km depth, before disappearing altogether at about 700-km depth. This cut-off of
521 seismicity roughly corresponds to modes M3 and M4 of ThERM (Patton and Watkinson, 2010).

522

523 In summary, many, but certainly not all, of the variations of earthquake depth-energy release from the CMT
524 catalog correspond with the boundary layer structure of ThERM (Patton and Watkinson, 2009, 2010)
525 (Table 3). The coincidence of inflections, triplications, and minima in these release curves with the

526 predicted depths of isobaric shearing modes suggests a coherent layering of thermomechanical competence
 527 with depth in the planet. Furthermore, the marked differences in event-normalized energy release between
 528 tectonic regions suggest significant lateral variations. Consequently, it makes sense to explore further the
 529 implications of this model for dynamic plate theory.

530

531 **3.0 Thermodynamics of solid self-gravitating matter configurations**

532 3.1 Preliminaries

533 The macroscopic notion of heat is defined as the difference between the internal energy and work
 534 performed on a system, consistent with the Joule heating experiments (Chandrasekhar, 1967). The First
 535 Law of thermodynamics is therefore

$$536 \quad dQ = dU - dW \quad (2)$$

537 where dQ , dU and dW are increments of heat, internal energy and work, respectively. Note that heat is a
 538 derived quantity, having no meaning independent of the First Law.

539

540 Guided by triaxial rock mechanics experiments, I shall account for the entropy density of strained solid
 541 materials using a simple one-dimensional elastic model. This model exhibits an unorthodox behavior
 542 consistent with Lavenda's (1995) notion of thermodynamic symmetry breaking. I deduce the expected
 543 slope, shape, and temperature dependence of the energy density for this model, which then serves as foil for
 544 the thermomechanics of shear localization exhibited by non-linear elastic DG-2 materials. Note that while
 545 entropy appears in all statements of the Second Law, it was first formulated axiomatically by Carathéodory
 546 (ca. 1909), based on an analysis of Pfaffian differential equations, to read

$$547 \quad dQ = TdS \quad (3)$$

548 where dS is an increment in the entropy density, and T is absolute temperature.

549

550 Consider a cylindrical test specimen of rock, with length l and diameter d , placed in a loading frame for the
 551 purpose of strength characterization. Upon applying a force φ directed along a line parallel to the
 552 specimen's length, it is observed that the specimen shortens by a length increment dl . Consequently, the
 553 increment of work needed to shorten the cylinder from $l+dl$ to l is given by

554
$$dW = \varphi dl . \quad (4)$$

555 Because the specimen can be held under relatively small loads for long periods of time, it is reasonable to
 556 assume that it manifests a force equal and opposite to the applied load. Presumably, this reaction force
 557 arises from electromagnetic interactions in the sample's microstructure. Furthermore, experience shows
 558 that if the cylinder were unloaded, it would likely return to its original length. This is Hooke's law (*Ut*
 559 *tensio sic vis*, ca. 1642).

560

561 However, it is equally valid to consider this problem from a material point of view. Responding to a
 562 directed environmental load of magnitude φ , the cylinder strains by an increment dl of its overall length l ,
 563 and as a result distributes an increment of energy dU throughout its microstructure and mineral fabric.

564 Therefore, I am also free to assume a macroscopic relation of the form

565
$$dU = \varphi dl . \quad (5)$$

566

567 From a thermodynamic point of view, the unloaded state to which the cylinder tends to return upon
 568 unloading is somehow more likely than the loaded one, and should therefore coincide with a maximum in
 569 entropy. Consequently, any deformation of the cylinder from this ideal state must necessarily decrease the
 570 entropy of the cylinder itself, as a function of length. Consequently, I seek a relation of the form

571
$$dS = -f(l)dl . \quad (6)$$

572 Combining the First and Second Laws, equations (2) and (3), I obtain

573
$$TdS = dU - dW . \quad (7)$$

574 Upon substituting for the work and internal energy increments using (4) and (5) respectively, I find

575
$$TdS = \varphi dl - \varphi dl \Rightarrow dS = 0 \quad (8)$$

576 Hence, for a positive absolute temperature thermodynamics predicts no increase in entropy, consistent with
 577 the apparent lack of energy dissipation, a state of mechanical equilibrium for cylinders under small loads,
 578 and everyday experience.

579

580

581 3.2 Strained inhomogeneous elastic solids

582 Curiously, there is no need to account for heat in these experiments, despite its fundamental importance in
 583 thermodynamics. It would appear that there is no meaningful distinction to be made between heat and
 584 work for this model (Lavenda, 1995). Instead the thermodynamic potentials for work, internal energy, and
 585 entropy are all functions of a single variable. This has immediate consequences for the usual combination
 586 of the First and Second Laws, equation (7). Because heat and work are indistinguishable, and heat is
 587 already accounted for in the product of the temperature and the entropy increment through the Second Law,
 588 equation (7) can be rewritten as

$$589 \quad \frac{f(l)}{\varphi} = \frac{1}{T} = -\frac{d\Delta S}{d\Delta U}. \quad (9)$$

590 Here the entropy and internal energy are prefixed with deltas to distinguish these *primitive functions* from
 591 the classical thermodynamic potentials assumed above, which are first-order homogeneous functions.

592 These primitive functions are *inhomogeneous*, which is to say that they can manifest scale-dependence,
 593 contrary to the scalability expected of classical homogeneous potentials. In the following section I explore
 594 the scale-dependence of this system, by employing power laws for initial statistical distributions in length.

595

596 The importance of statistical variability in the behavior of elastic materials, and rocks in particular, is
 597 demonstrated by modeling the entropy and energy potentials for this system as power laws in length l .

598 Following Lavenda (1995), I define the *internal energy increase* as

$$599 \quad \Delta U(l) = \frac{\eta}{m} l^m \quad (10)$$

600 and the *entropy reduction* as

$$601 \quad \Delta S(l) = -\frac{k\sigma}{n} l^n \quad (11)$$

602 where k is Boltzmann's constant, σ and η are positive constants independent of temperature, and n and m
 603 are positive numbers.

604

605 Observe that equation (9) can be rearranged to represent the temperature as

606
$$T = -\frac{d\Delta U}{d\Delta S}. \quad (12)$$

607 Upon differentiating the primitive functions (10) and (11) with respect to length, and substituting into
 608 equation (12) I obtain

609
$$T = \frac{\eta}{k\sigma} l^{m-n}. \quad (13)$$

610 Consequently, the temperature of this model system can either increase or decrease with length, depending
 611 on whether the exponent $m - n$ is positive or negative. The temperature is independent of length for $m = n$.

612

613 The modulus of elasticity E for the model is defined by the derivative of the force ϕ , which in turn is the
 614 derivative of the internal energy, equation (5). Upon eliminating length in this expression via the
 615 temperature relation, equation (13), I obtain

616
$$E = (m-1)\eta \left(\frac{k\sigma T}{\eta} \right)^{\frac{m-2}{m-n}}. \quad (14)$$

617 For $n = 2$, the modulus of elasticity is $E=(m-1)k\sigma T$, and the force reduces to a generalized Hooke's law
 618 $\phi=E(T)l$. This relation further reduces to a linear force-displacement law, but only when the internal
 619 energy too is quadratic in length, $m = 2$.

620

621 Upon inverting equation (13) to express length as a function of temperature, differentiating the result with
 622 respect to temperature, and eliminating the constants via (13) I obtain

623
$$\frac{1}{l} \frac{dl}{dT} = \frac{1}{(m-n)T}. \quad (15)$$

624 This expression characterizes the thermal elongation of the model, analogous to the thermal expansivity in
 625 three-dimensions. The latter material property dictates the scale over which body forces can act in the
 626 model. Consequently the model elongates upon heating for $m > n$, shortens upon heating for $m < n$, and is
 627 undefined for $m = n$.

628

629 By separating the entropy and energy increments in equation (12), dividing through by a temperature
 630 increment dT , and employing the chain rule to express the common length dependencies for entropy,
 631 energy, and temperature, I obtain

$$632 \quad \frac{d\Delta U}{dl} \frac{dl}{dT} = -T \frac{d\Delta S}{dl} \frac{dl}{dT}. \quad (16)$$

633 Upon substituting the derivatives of equations (10), (11), and (13) with respect to length into (16) I find

$$634 \quad \frac{d\Delta U}{dT} = -T \frac{d\Delta S}{dT} = \left(\frac{\eta}{m-n} \right) \frac{l^m}{T} \quad (17)$$

635 For positive absolute temperature, this shows that the heat capacity of this inhomogeneous elastic system
 636 cannot be defined simultaneously as

$$637 \quad C \equiv \frac{dQ}{dT} = T \frac{d\Delta S}{dT} \quad (18)$$

638 and

$$639 \quad C \equiv \frac{dQ}{dT} = \frac{d\Delta U}{dT} \quad (19)$$

640 because one of these definitions always will be negative when the other is positive, and *vice versa*. Apart
 641 from the pathological case for $m = n$, there are two other distinct types of inhomogeneous elastic systems
 642 depending on whether $m < n$ or $m > n$.

643

644 Variability as a function of length is inversely proportional to the exponent appearing in the primitive
 645 power laws, above. Hence, a smaller exponent means greater variability. Equation (10), defining the
 646 internal energy increase, is associated with *mechanical* variability. However, equation (11), defining the
 647 entropy reduction, is associated with *statistical* variability rather than thermal variability, because heat is
 648 not evident in this problem. Consequently, systems dominated by either mechanical variability ($m < n$) or
 649 statistical variability ($m > n$) can be identified on the basis of their heat capacity C , as follows:

$$650 \quad C \equiv \frac{dQ}{dT} = \begin{cases} T \frac{dS}{dT}, m < n \\ \frac{dU}{dT}, m > n \end{cases} \quad (20)$$

651 These conclusions are easily substantiated by returning to thermodynamic fundamentals. Eliminating
 652 length between the primitive equations (10) and (11), I find for the case of mechanical variability that

$$653 \quad \Delta S \sim -(\Delta U)^{\frac{n}{m}}. \quad (21)$$

654 In words, the *entropy* is a *concave function* of the internal energy. Also, for the case of statistical
 655 variability I find that

$$656 \quad \Delta U \sim (\Delta S)^{\frac{m}{n}}. \quad (22)$$

657 In words, the *internal energy* is a *convex function* of the entropy. Furthermore, because $dS/dU < 0$, these
 658 representations are mutually exclusive. The usual symmetry of the entropy and energy representations,
 659 expected from equilibrium thermodynamics and arising from first-order homogeneity of thermodynamic
 660 potentials, is broken.

661

662 For an inhomogeneous elastic system dominated by *mechanical variability* ($m < n$), dQ is the amount of
 663 heat *evolved* by the system, which leads to a decrease in entropy by an amount $dS=dQ/T$ (Figure 6a).

664 Therefore fewer microscopic states are available at lower temperatures. The slope of the concave entropy
 665 density function is $-1/T$; higher temperatures are associated with flatter slopes, and lower temperatures with
 666 steeper slopes. This model elongates upon cooling. Because temperature and heat are both decreasing
 667 functions of length, the entropy density is proportional to length. Mechanical variability offers no insight
 668 for the thermodynamics of DG-2 materials.

669

670 On the other hand, in an inhomogeneous elastic system dominated by *statistical variability* ($m > n$), dQ is
 671 the amount of heat *absorbed* by the system, which leads to an increase in internal energy by an amount dU
 672 $= dQ > 0$ (Fig. 6b). This corresponds to a decrease in the entropy by an amount $dS = -dQ/T$. Consequently
 673 there are fewer microscopic states available at higher temperatures. The slope of the convex energy density
 674 function is $-T$; higher temperatures are associated with steeper slopes, and lower temperatures with flatter
 675 ones. This model elongates upon heating. Furthermore, because temperature and heat are both increasing
 676 functions of length, energy density is inversely proportional to length. Statistical variability offers crucial
 677 insights for the thermodynamics of DG-2 materials.

678

679 Nowhere in this simple one-dimensional model has the phenomenon of shear failure been addressed. For
 680 example, if we repeatedly load our test specimen, or apply progressively higher loads, experience tells us
 681 that the specimen will, at some point, spontaneously fail, sometimes after suffering significant
 682 microphysical damage (Katz and Reches, 2004). In other words, the simple act of loading the test cylinder
 683 changes its prior microstructure and mineral fabric. Although the detailed distribution of these changes
 684 cannot be known to an outside observer, they can be treated statistically, as was appreciated by Weibull (ca.
 685 1939). These issues are addressed in Section 4.0.

686

687 3.3 Self-gravitating matter configurations

688 Lavenda (1995) shows that the thermodynamics of a self-gravitating body, like a planet or star, is also
 689 subject to symmetry breaking of the type outlined above. In this case, like that of inhomogeneous elastic
 690 systems dominated by statistical variability, the energy density is given by a monotonically decreasing
 691 function of the entropy density (Figure 6b). Significantly, the energy density is inversely proportional to
 692 the body's radius. In other words, both pressure and temperature increase with depth.

693

694 The heat capacity of a self-gravitating body is defined by

$$695 \quad C \equiv \frac{dQ}{dT} = \frac{dU}{dT} = \frac{mc^2}{T_0} \quad (29)$$

696 where m is the mass of an elementary particle, c is the speed of light, and T_0 is a reference temperature.

697 The energy density, and by association the stress, of a self-gravitating body plays a fundamental role in
 698 shaping the body, and in controlling its spacetime evolution, in accordance with the far reaching
 699 implications of Einstein's (1916) theory of gravitation.

700

701 **4.0 Thermomechanics of DG-2 materials**

702 4.1 Diharmonic equation

703 The pure-shearing plane-strain deformation of non-linear elastic DG-2 materials is governed by the
 704 diharmonic equation (Patton, 1997)

705
$$0 = \alpha^2 \frac{\partial^4 \psi}{\partial x^4} + (1 + \alpha^2) \frac{\partial^4 \psi}{\partial x^2 \partial z^2} + \frac{\partial^4 \psi}{\partial z^4} \quad (24a)$$

706
$$\alpha^2 = (1 - 2(\kappa/\chi))/(1 + 2(\kappa/\chi)) \quad (24b)$$

707 where the ratio of thermal κ to mechanical χ diffusivities is called thermomechanical competence. Note
 708 that as $\kappa/\chi \rightarrow 0$, equation (24) reduces to the biharmonic equation, which appears in theories of linear
 709 elastic and linear viscous materials.

710

711 4.2 Incipient modes analysis

712 Here incipient modes analysis (Patton and Watkinson, 2010) is used to document the deformation modes of
 713 DG-2 materials and thereby facilitate comparison with the thermodynamic properties of simple
 714 inhomogeneous elastic materials, documented in section 3. I substitute wave-like harmonic and
 715 dislocation-like shear band solutions into the differential equation (24) to identify domains where
 716 deformation modes of these types are possible. In all cases, domains of thermomechanical competence that
 717 allow real roots, or at least roots with real parts, will admit solutions of the assumed type. In both trial
 718 solutions ψ is the stress-energy function, identically satisfying incompressibility. This linear analysis in no
 719 way constrains the finite growth of the resulting structures.

720

721 For these analyses, consider a two-dimensional spatial domain in which a specific but arbitrary set of
 722 Cartesian axes are drawn through an arbitrarily chosen point. Consider also a plane strain deformation field
 723 where the velocity components (u, w) expressed in this coordinate system are assumed proportional to the
 724 distance from the origin in the following way, $(u, w) \propto (-x, z)$.

725

726 The usual Cartesian harmonic normal modes

727
$$\psi = \exp^{i\alpha x + rz} \quad (25)$$

728 suffice for the wave-like case. Here a relatively competent layer of thickness H^* has its mean position
 729 parallel to the shortening direction, and it is initially planar. In other words, the boundaries between the
 730 layer and the weaker matrix initially lie at $z = \pm H^*/2$. As the layer shortens in the base field, it tends to

731 thicken, and harmonic perturbations with amplitude δ^* might begin to develop. The growth of such
 732 undulations into observable folds or waves depends on the relative rates of their amplification versus
 733 uniform layer thickening. The wavenumber ω predicts the normalized wavelength of the incipient
 734 undulation through the relation $L^*/H^* = 2\pi/\omega$. The small scalar parameter in this case is $\varepsilon = \delta^*/H^*$, so that
 735 these deductions are rigorous only for the case of infinitesimal fold amplitude.

736

737 Substituting the harmonic trial solution (25) into (24a) I obtain the four distinct roots

738
$$r = \pm\omega \quad \text{or} \quad r = \pm\alpha\omega . \tag{26}$$

739 These are all real for $0 < \kappa/\chi < 1/2$, thus wave-like material deformations are expected to form on this
 740 domain of relatively low thermomechanical competence, in response to far-field forcing (Figure 7a, solid
 741 blue curve). Note also that for $1/2 < \kappa/\chi < \infty$ these roots are mixed, with two real and two pure imaginary, so
 742 that harmonic disturbances are also possible on this domain of higher thermomechanical competence
 743 (Figure 7a, dotted blue curve). Together, these harmonic perturbations represent shear waves (reversible
 744 rotational distortions) propagating throughout the material (Truesdell, 1964). Furthermore, given the
 745 planetary scale implications of DG-2 thermodynamics, material coupling on the domain of lower
 746 competence could explain some aspects of long-period Love wave attenuation in the upper mantle (Table
 747 5). The normalized wavelength of these disturbances scales as $L^*/H^* = (\kappa/\chi)^{-1}$ (Patton and Watkinson,
 748 2005).

749

750 In the dislocation-like case, I use shear band solutions

751
$$\psi = \exp^{g_z x - g_x z} \tag{27}$$

752 following the work of Hill & Hutchinson (1975) and Needleman (1979). The vector \mathbf{g} , with components g_x
 753 and g_z in the chosen coordinate system, is normal to the incipient shear band. Consequently, the arctangent
 754 of the (real) ratio g_x/g_z determines the angle between the band itself and the shortening direction. The ratio
 755 of the thickness of the incipient band δ^* , to its length L^* , provides a suitable small scalar parameter ε , so
 756 that these deductions are rigorous only for the case of a vanishingly thin band.

757

758 Substituting the shear band trial solution (27) into (24a), I obtain the four distinct roots

$$\frac{g_x}{g_z} = \pm i \quad \text{or} \quad \frac{g_x}{g_z} = \pm i \alpha . \quad (28)$$

760 While the first pair of roots is purely imaginary, the second pair is real for $\frac{1}{2} < \kappa/\chi < \infty$, where the rescaling
 761 modulus (24b) itself is imaginary. Consequently, dislocation-like disturbances are expected to form at
 762 angles, symmetric about the loading axis, ranging from 0 to 45 degrees for these relatively high values of
 763 thermomechanical competence (Fig. 7a, red curves). Significantly, an angle of 30 degrees corresponds
 764 with the value $\kappa/\chi = 1$, which defines the lower limit of thermomechanical rigidity. This suggests that
 765 dislocation-like disturbances should form, preferentially, at about 30 degrees with respect to the shortening
 766 direction in thermomechanically competent materials (Patton and Watkinson, 2011; Patton and Watkinson,
 767 in review). This prediction is consistent with Anderson's 1905 theory of crustal faulting (Jordan et al.,
 768 2003).

769

770 4.3 Stress-energy density map

771 The thermomechanics of DG-2 materials can be represented graphically (Patton, 2005; Patton and
 772 Watkinson, 2005) (Figure 7b) using three energy thresholds, one for distributed harmonic deformations
 773 (green curve, $\psi^D = (\kappa/\chi)^{-1}$), one for intrinsic strain-energy storage (gray curve, $\psi^I = (|\alpha|)^{-1}$), and another for
 774 localized shearing deformations (orange curve, $\psi^L = (|\alpha|\kappa/\chi)^{-1}$). Taken together, these curves define a
 775 statistically stable stress-energy density map for these materials. Observe that the three threshold curves
 776 are monotonically decreasing on certain domains of thermomechanical competence, and that the stress-
 777 energy density approaches infinity ("blows up") at the lower end of these respective domains. The
 778 distributed threshold curve has a vertical asymptote at $\kappa/\chi = 0$, while the intrinsic curve has one at $\kappa/\chi = \frac{1}{2}$.
 779 The localization threshold curve, defined as the product of the other two, consequently exhibits two
 780 asymptotes, with a distinct non-zero energy minimum between them. The presence of two distinct energy
 781 spikes in this diagram, and their diffusive connection via the dynamic rescaling theorem (Patton and
 782 Watkinson, 2010), give rise to all of the geologically interesting behavior of the DG-2 material.

783

784 **5.0 Application to rock mechanics**

785 The foregoing analysis can be applied to the interpretation of data from rock mechanics experiments on
 786 cylindrical specimens. Three facts make this possible. First, the earlier analysis of statistical variability
 787 (Figure 6b) shows that the energy density for strained elastic solids must be a monotonically decreasing
 788 function of the entropy, which in turn must be an inverse function of length. Thus, the diameter/length
 789 ratio (d/l) of a cylindrical specimen serves as the abscissa for plotting these data (Table 6). Second,
 790 because the intrinsic stress-energy density threshold (ψ^l , Figure 7b) arises from the differential normal-
 791 stress term of the DG-2 constitutive equation (Patton, 1997; Patton and Watkinson, 2005; Patton and
 792 Watkinson, 2010; Patton and Watkinson, 2011) it makes sense to plot normalized differential stress (NDS)
 793 from the experiments as the ordinate. Using Katz & Reches' (2002, 2004) definition of $NDS = (\sigma_1 - \sigma_3)/586$
 794 and *their* identification of $NDS \sim 0.96$ as a critical threshold for spontaneous sample failure, it is a simple
 795 matter to see that the number $\zeta = 4\sqrt{3}$, common in the theory of DG-2 materials (Patton and Watkinson,
 796 2010), reconciles their conclusion with this thermomechanical theory. The final and seemingly obvious
 797 fact is that the deformation of any rock sample in any load frame is possible only because of the
 798 *thermomechanical rigidity* of the loading frame itself. Thus, the deformed samples and the loading frame
 799 comprise complementary parts of a larger, and more interesting, thermomechanical system. The samples
 800 plot at $(\kappa/\chi, \psi) = (d/l, \zeta (\sigma_1 - \sigma_3)/586)$, while the loading frame plots at $(\kappa/\chi, \psi) = (1, 1)$.

801

802 Fourteen samples of the medium-grained Mt. Scott granite were loaded to predetermined values of axial
 803 stress σ_1 , at confining pressure $\sigma_3 = 41$ MPa, and held for predetermined periods, before the loads were
 804 slowly released. Twelve samples that did not suffer macroscopic failure are plotted as green circles (Figure
 805 7b). Three of these samples (105, 124, & 125, Figure 7b, inset) were reloaded to failure at higher loads, as
 806 indicated by gold diamonds and thin dashed lines. Three other samples loaded to failure also are plotted as
 807 gold diamonds. Three samples (#104, # 106 and #110), plotted as red diamonds, spontaneously failed
 808 during their hold periods. Given the standard error in measured Coulomb strength for the Mt. Scott granite
 809 (586 ± 16 MPa), indicated by the thin dashed lines plotted above and below the distributed and localized
 810 threshold curves (inset), all the failed samples plot above the localization threshold.

811

812 Katz & Reches (2002, 2004) observed the microscopic and macroscopic damage to several samples after
 813 loading. They report two populations of microscopic cracks. Population A are intragranular tension cracks
 814 (Figure 7a, red dashed curve) with angles, in relation to the loading direction, in the range $0^\circ - 10^\circ$, while
 815 Population B are intergranular shear fractures (Figure 7a, red solid curve) with angles in the range $11^\circ -$
 816 40° . They also report angles of macroscopic shear failures, which tend to increase with confining pressure.
 817 The macroscopic shear angles correspond to thermomechanical competences in the range $0.6 < \kappa/\chi < 0.9$.
 818 These values are consistent with ‘internal friction’ values for Anderson-type brittle faulting. Additionally,
 819 the angle of the macroscopic shear developed in specimen #110, which suffered spontaneous failure during
 820 its hold period, can be connected to its pre-failure loading state by a tie line LB-LY’, tangent to the
 821 localization curve. Thus, the macroscopic failures observed in these triaxial loading experiments appear to
 822 be consistent with the predictions of dynamic rescaling (Patton and Watkinson, 2010). In contrast, the
 823 microscopic Population B shear fractures correspond to the range $0.54 < \kappa/\chi < 2.9$. This spread might
 824 reflect the inhomogeneous distribution of lengths in the samples prior to loading, the effect of confining
 825 pressure, or both.

826

827 Data from the three spontaneously failed samples can be used to estimate the mechanical diffusivity as $\chi =$
 828 l^2/τ . The resulting values fall in the range $2.3 \leq -\log \chi \leq 5.6$. These estimates are in or below the range $-\log$
 829 $\chi \leq 5.3-5.7$, predicted by theory (Patton and Watkinson, 2010), and overlap with ranges estimated from
 830 GPS strain rates, $4.3 \leq -\log \chi \leq 7$, GPS differential velocities, $4.4 \leq -\log \chi \leq 5.2$, and structural data, $4.2 \leq -$
 831 $\log \chi \leq 4.7$. This correlation suggests that combined analysis of data from experimental rock mechanics
 832 and GPS surveys will factor highly in further development of dynamic plate theory.

833

834 **6.0 Isobaric shearing hypothesis**

835 In a self-gravitating fluid body, pressure p increases with depth according to the hydrostatic relation $p =$
 836 ρgz , where ρ is mass density, g is gravitational acceleration, and z is depth. Similarly, pressure increases
 837 with depth in a solid body according to a lithostatic relation, given by the tensor trace of its stress-energy
 838 density. The depth to which differential stresses can persist in any planet, then, depends on the definition
 839 of its stress-energy density. However, because even terrestrial planets are spheroidally-shaped, which

840 reflects the combined effects of their self-gravity and rotational momentum, the magnitude of these
841 differential stresses must be small. Furthermore, given that temperature increases with depth (Figure 6b),
842 and that microphysical mechanisms for solid-state creep are thermally activated, even these small
843 differential stresses must diminish rapidly with depth. In the static case, they decay entirely, and the
844 pressure becomes for all intents and purposes hydrostatic. Consequently, the maintenance of differential
845 stresses at depth in a planet requires some dynamic process (McKenzie, 1967). For more than 40 years,
846 this process has been assumed to conform to the assumptions of the standard Earth model (Bercovici et al.,
847 2000; Bunge et al., 1997; Tackley, 2000). However, based on the foregoing thermomechanical analysis, it
848 is likely that geodynamics is much more interesting than heretofore recognized.

849

850 With pressure and temperature as boundary conditions on a self-gravitating planet, and confining pressures
851 much larger than potential differential stresses, it is hard to argue that material strength matters, except for
852 the fact that the *dynamic rescaling theorem* (Patton and Watkinson, 2010) focuses deformation on the
853 smallest crystalline structures of a solid system. This is necessary, so that the global dissipation of energy
854 is minimized. An immediate consequence of this prediction is that shear waves can be propagated
855 throughout a thermomechanical mantle, whereas in a viscous one, no such propagation is possible. Absent
856 this theorem, however, one must accept the geodynamicist's approximation, that over long time and length
857 scales the mantle is effectively viscous. As plausible as this might sound, it is impossible to falsify.
858 Moreover, it is inconsistent with the fact that rocks loaded in the laboratory exist in the solid-state. Thus, it
859 is clear that the failure of the standard Earth model arises solely from a theoretical deficiency. On the other
860 hand, with the dynamic rescaling theorem, the only substantive differences between deformation of a rock
861 sample in the laboratory, and tectonic deformation of the Earth, are the relative magnitude of the confining
862 pressure and effect of global conservation laws. In other words, shear localization at the planetary-scale
863 must account for the incompatibility of rectilinear motions with the spheroidally curved geometry of the
864 planet itself, while in the laboratory this is of no concern.

865

866 The statistically stable thermomechanics of non-linear elastic DG-2 materials are not altered by pressure.
867 Consequently, even under extreme pressures the locus of its three energy thresholds and documented

868 scaling relationships can be expected to hold. Therefore, a thermomechanical Earth model can be formed
869 simply by scaling up to Earth's radial structure and applying pressure and temperature boundary conditions
870 at its surface (Patton and Watkinson, 2009, 2010). The result (Figure 8) immediately predicts a variation of
871 pressure and temperature expected for Earth's mantle. Furthermore, it predicts that the outer colder parts of
872 the mantle should be thermomechanically rigid, thermodynamically isothermal, and subject to brittle shear
873 localization, while the deeper hotter parts should be thermomechanically ductile and thermodynamically
874 adiabatic. Adiabaticity prevails as $\kappa/\chi \rightarrow 0$, consistent with depths in the lower mantle, and coincidentally
875 where Birch (1952) showed it to pertain on the basis of seismic wave speed variations (Equation 1). The
876 asthenosphere of a thermomechanical Earth is not adiabatic, because differential stresses (normal stress
877 differences) there are large enough to cause shear localization. Moreover, the vanishing of seismicity at the
878 asthenosphere-mesosphere boundary, ~ 700 km deep, reflects this fundamental change in thermodynamic
879 conditions. For comparison, the variation in earthquake depth-energy release (Figure 5) is plotted in the
880 last panel of Figure 8, where the most significant deviations from the per-event global baseline clearly
881 correlate with the low velocity zone, and depths consistent with Earth's lithosphere and tectosphere.

882

883 This model, being self-similar or fractal, can also be used to correlate crustal and upper mantle
884 observations. Figure 9 depicts 'crustal overtones' of ThERM. For comparison, the variation in earthquake
885 depth-energy release for all six margin types considered in this paper (Figure 4) are plotted in the last panel
886 of Figure 9, where the most significant deviations from the global per-event baseline correlate to the
887 seismic lid and crust. What does this remarkable correlation mean for dynamic plate theory?

888

889 For a self-gravitating solid elastic body, like a terrestrial planet, we can anticipate some degree of interplay
890 between the inhomogeneous statistical distribution of length scales in the body, and the distribution of
891 thermal and compositional lengths over which the body force of gravity might act. This interplay is
892 expressed particularly in the structure of the thermomechanical boundary layer that forms adjacent to the
893 cold surface of the planet, but also by the fact that elastic shear waves are propagated throughout the
894 mantle. Thus, in order for any portion of a thermomechanical planet to suffer deformation, there must be
895 measurable contrasts in material competence, as well as concentrated body forces. Furthermore, the

896 mechanical diffusivity χ must be greater than the thermal diffusivity κ in deforming portions of this
897 complex system. Consequently, the thermomechanical boundary layer that forms will always be ζ times
898 thicker than the purely thermal one. Depth variations in seismic energy release on such a planet are
899 therefore to be expected. Finally, given that pressure and temperature variations are explicitly predicted by
900 theory, it is reasonable to suppose that variations in material competence will exhibit strong dependencies
901 on bulk composition and volatile content.

902

903 In summary, the energy density function for a self-gravitating, inhomogeneous elastic body, dominated by
904 statistical variability ($m > n$), must be a monotonically decreasing convex function of the radial coordinate
905 and the entropy reduction. Furthermore, the entropy reduction itself is an inverse function of length. Heat
906 absorbed by such a system will tend to increase the internal energy, but correspondingly decrease the
907 entropy. Such a body will not readily evolve heat, except when regional conditions favor a return to more
908 classical thermodynamics. In these subsystems, the energy density function would necessarily exhibit a
909 positive slope. The monotonically increasing branches of the intrinsic and localization thresholds (dashed
910 curves, Figure 7b) exhibit these characteristics, and also correlate with depths in the asthenosphere where
911 magma generation generally is thought to take place (Figures 8 and 9). Magmatic differentiation provides a
912 mechanism for generating density contrasts between continental and oceanic crust, the tectosphere, and
913 average mantle.

914

915 These considerations are quite general and place, once and for all, the stress-energy density thresholds of
916 DG-2 materials (Patton and Watkinson, 2005) in a coherent thermodynamic context. Consequently, the
917 behavior of these ideal materials can be correlated with the pressure, temperature, age, and geometry of
918 geological structures observed in outcrops, orogens, and terrestrial planets. For example, the outer parts of
919 such planets are predicted to be relatively cold, competent, and subject to dynamic shear localization
920 (“brittle”), while the inner parts are predicted to be relatively hot, incompetent (“ductile”), and structurally
921 simple. For Earth, this is reflected in the remarkable correlation of spherically symmetric elastic models,
922 like PREM (Dziewonski and Anderson, 1981), with the predicted depth distribution of isobaric shears in a
923 body with a ~100-km thick lithosphere (Patton, 2001; Patton and Watkinson, 2009, 2010). As

924 demonstrated here, this correlation also holds for variations in earthquake depth-energy release (Figures 3-
 925 5). The following section discusses the implications of these findings for the interpretation of various
 926 geophysical data sets, and dynamic plate theory in general.

927

928 **7.0 Discussion**

929 7.1 Laboratory measured versus theoretical viscosity

930 Spontaneous shear dislocations are characteristic modes of deformation for solids under loading, which are
 931 related non-linearly to the strength of the loaded material. In a loading frame in the laboratory, rock
 932 strength can be reduced to a steady-state rate of energy dissipation in shear, i.e. ‘viscosity’. This is possible
 933 only because the loading frame itself is effectively rigid (‘stiff’) by comparison. But workers conducting
 934 these experiments, and theoreticians interpreting their results for geodynamic models, surely understand
 935 that the materials involved are solids. So why is the standard Earth model based on viscous fluid
 936 dynamics?

937

938 Another important macroscopic property of rocks is density, which is related to chemical composition and
 939 mineralogy via specific gravity. Perhaps, then, a better measure of rock ‘strength’ is the ratio of a rock’s
 940 ‘viscosity’ to its density. This ratio has dimension $\mathcal{L}^2\mathcal{T}^{-1}$, which has been called ‘diffusivity’. This latter
 941 term is descriptive, in that energy is being dissipated by the imposed deformation, and unburdened by the
 942 fluid mechanical connotations of the term ‘viscosity’.

943

944 For example, the rate of energy dissipation in the shearing of a rheological fluid depends on the ratio of its
 945 molecular viscosity (μ) and its density (ρ). Although we might call this quantity the ‘shear stress
 946 diffusivity’, one usually hears the term *kinematic viscosity* ($\nu = \mu/\rho$).

947

948 Similarly, the rate of heat dissipation in a substance can be expressed as the ratio of its thermal conductivity
 949 (k) to the product of its heat capacity (C_p) and density (ρ), also having dimension $\mathcal{L}^2\mathcal{T}^{-1}$. This quantity is
 950 usually called *thermal diffusivity* ($\kappa = k/\rho C_p$), but perhaps some would prefer the term ‘thermal viscosity’?

951

952 Finally, the rate of energy dissipation in a deforming rheological solid can be expressed as the ratio of its
953 ‘viscosity’ to its density, which might also be called ‘kinematic viscosity’. However, because this brings to
954 mind many ideas that have naught to do with deforming solids, it does little to dispel the lexical confusion I
955 am attempting to address. Consequently, based on my study of DG-2 materials, I suggest the term ‘normal-
956 stress diffusivity’. However, in a pinch one might simply try *mechanical diffusivity* ($\chi = d^2/\tau$), as it
957 provides a descriptive counterpoint to the thermal diffusivity, above. Semantics aside, the crucial thing
958 here is that geologists acknowledge the fundamental theoretical difference between the mode of energy
959 dissipation in rheological fluids, and the possible modes of energy dissipation in rheological solids. The
960 theory discussed here is parameterized by the ratio κ/χ , which might be called *thermomechanical*
961 *competence*. Regardless of its name, it provides new insight into the nature of Earth’s plate-like blocks,
962 and their relative horizontal and vertical motions.

963

964 7.2 Implications

965 There are good reasons to think that the observed earthquake depth-energy release signal is real. First,
966 while it is known that hypocenter locations are strongly influenced by reference model, centroid locations
967 are not. This is because hypocenter locations are triangulated using body wave travel times, while
968 centroids are located using a summation of long-period body wave and free-oscillation modes. In fact, the
969 relocation algorithm for centroids is remarkably insensitive to small scale *a priori* structure (Aki and
970 Richards, 2002). Furthermore, earthquakes are but one, relatively minor, mode of energy dissipation for
971 the planet, and hence must at some level be related to more general deformation processes in a self-
972 gravitating body (Chao and Gross, 1995; Chao et al., 1995). If the observed coincidence between the
973 earthquake depth-energy release curves and ThERM is real, then it provides crucial support for the
974 hypothesis that Earth's tectonic plates are part of a thermomechanical boundary layer, as much as 700-km
975 thick, that has developed over the course of Earth's history (Patton, 2001; Patton and Watkinson, 2009).

976

977 This coincidence has interesting implications for post-orogenic extensional collapse of orogens, particularly
978 when compared with recent reviews of pressure-temperature-time paths for metamorphic rocks. Maximum
979 pressure estimates, based on equilibrium mineral phase assemblages, for mid-crustal schists and gneisses

EARTHQUAKE DEPTH-ENERGY RELEASE

980 also commonly coincide with ThERM shear modes (Brown, 2007). A striking example of this is the depth-
981 pressure classification of detachment faults exposed in metamorphic core complexes in the northwestern
982 United States and southwestern Canada, where maximum pressures coincide with H4, L1, and L2 (Patton
983 and Watkinson, in review).

984

985 If observed variations in earthquake depth-energy release are interpreted as a proxies for strength, or more
986 specifically for depth and lateral contrasts in thermomechanical competence (κ/χ), then the weakest parts of
987 the crust globally are located between 15- and 25-km depths (Figure 3b). Regionally the weakest crust is
988 found in continental transform, oceanic ridge/transform, continental rift, and Himalayan-type convergent
989 margins (Figures 4, 5). The appearance of ocean crust in this list probably reflects its relative thinness,
990 rather than its intrinsic weakness. The upper and lower boundaries of this weak layer occur at depths
991 consistent with predicted shearing modes H4 and L1 of ThERM (Patton and Watkinson, 2010). Finally,
992 there are additional triplications and slope changes at about 37-km depth, coincident with mode L2 of
993 ThERM, also suggestive of a vertical change in thermomechanical competence. As mentioned above,
994 metamorphic tectonites with pressures of this magnitude are common in collapsed orogens (Brown, 2008).
995 It is likely that the integration of crustal pressure-temperature-time data with centroid moment release
996 studies at a regional scale will be a potentially fruitful avenue for future research.

997

998 Significant differences in the number of hypocenters and centroids occur to about 40-km depth (Table 2).
999 This simply reflects the depth range most affected by the procedural relocation of events in the CMT
1000 catalog. However, tectonically notable differences exist between the map and depth distributions of
1001 hypocenters and centroids above about 25-km depth, roughly coincident with mode L1 of ThERM (Patton
1002 and Watkinson, 2010). Centroids populate both convergent and divergent margins throughout this typical
1003 'crustal' depth range. In contrast, hypocenters largely occur above 15-km depth, with rare events as deep as
1004 25 km at divergent margins. Taken together, these distributions suggest a global maximum seismogenic
1005 crustal thickness of about 25 km (Figure 4a, b).

1006

1007 Using a thermal diffusivity of $10^{-6} \text{ m}^2\text{s}^{-1}$, typical for silicates (Vosteen and Schellschmidt, 2003), the
1008 equivalent thermal age for the 25-km-thick seismogenic crust is about 20 Ma. Presumably, this is the time
1009 needed for decompression melting processes at oceanic ridges to settle down to a steady-state (Crosby et
1010 al., 2006). Recent estimates of pressure and temperature ranges for MORB extraction, based on natural
1011 compositions, are about 1.2-1.5 GPa and 1250-1280 °C (Presnall and Gudfinnsson, 2008). These pressures
1012 correspond to depths of about 40-50 km, consistent with the depth extent of seismic energy release at
1013 oceanic ridges (Figure 4a, orange curve). Furthermore, these workers propose that fracturing of newly
1014 formed lithosphere induces the explosive formation and escape of CO_2 vapor, which drives MORB
1015 volcanism, while the source region for material forming the oceanic lithosphere extends no deeper than
1016 about 140 km. In this and other models, the MORB source region therefore lies comfortably below L2.
1017
1018 Hypocenters and centroids are common in the Alpine-Himalayan belt to depths of about 100 km, roughly
1019 coincident with mode L4 of ThERM, with rare events as deep as about 172 km, coincident with mode M1.
1020 Events beneath the Hindu-Kush occur to about 260-km depth, consistent with mode M2. All events deeper
1021 than about 260 km appear to be associated with down going slabs from past or present subduction of
1022 oceanic lithosphere. Note also that anelastic tomography (Romanowicz, 1994) reveals significant lateral
1023 variations in the attenuation of shear waves in the uppermost 250 km of the mantle, which are correlated
1024 with oceanic ridges and continental shields. The shear attenuation pattern below this depth apparently
1025 shifts, correlating with the global distribution of volcanic hotspots. Consequently, regions of Earth's
1026 asthenosphere underlying oceanic ridges and hotspots attenuate more low-frequency seismic energy than
1027 do cratons and shields, which can remain seismically active to similar depths. This is the same depth range
1028 as that potentially impacted by material coupling of surface waves in the thermomechanical boundary layer
1029 of ThERM (Table 5).

1030

1031 Using a typical thermal diffusivity of $10^{-6} \text{ m}^2\text{s}^{-1}$, the equivalent thermal ages for 100-km thick lithosphere,
1032 172-km thick upper tectosphere, and 255-km thick lower tectosphere are about 310 Ma, 940 Ma and 2Ga,
1033 respectively. In contrast, the equivalent *thermal* age for a layer 690-km thick is about 15 Ga, more than
1034 three times the age of the Earth and comparable to the age of the universe. Clearly, it is implausible that

EARTHQUAKE DEPTH-ENERGY RELEASE

1035 the structure of the asthenosphere is solely due to thermal diffusion processes. Consequently, some dynamic
1036 convective (advective?) process is needed to maintain differential stresses to these depths (McKenzie,
1037 1967).

1038

1039 Geologic history has been divided into ocean basin time (0-200 Ma), plate tectonic time (200-950 Ma), and
1040 “pre-tectonic” time (950-2300 Ma), on the basis of marine and continental geology (Moore and Twiss,
1041 1995). Also, based on Brown's (2008) recent review, the equivalent thermal ages, above, correspond to the
1042 amalgamation times for supercontinents Pangea, Rodinia, and Nuna. Reconciling the global smoothness of
1043 thermal (and viscous) diffusion with the spatial complexity and local non-smoothness of tectonic
1044 deformation processes requires a model that incorporates a self-consistent mechanism for strain localization
1045 with depth. Isobaric shearing in the asthenosphere offers a more comprehensive explanation for these first-
1046 order observations, than does the standard Earth model. It is time for the strength of solid earth materials to
1047 be included in dynamic plate theory.

1048

1049 As noted in Section 1.0, the spectral characteristics of Earth's gravity-topography correlation and
1050 admittance, combined with the adiabaticity of the lower mantle, are consistent with vigorous convection in
1051 the sublithospheric mantle of the standard Earth model, at lateral scales $\lambda_{1/2} > 1000 \text{ km}$. This conclusion
1052 complements those of regional isostasy, where near surface loads are supported by the flexural rigidity of
1053 the crust and lithosphere, at lateral scales $\lambda_{1/2} < 1000 \text{ km}$. This latter range of wavelengths, down to about
1054 50 km, has been called the ‘diagnostic waveband of flexure’ ((Watts, 2001), pg. 178). Furthermore, the
1055 inviscid (i.e., mechanically indeterminate) nature of the asthenosphere in flexural isostasy does not conflict
1056 with the fluid nature of the sublithospheric mantle in the standard model. Consequently, it is reasonable to
1057 conclude that mantle convection actively supports Earth's longest-wavelength gravity and geoid anomalies
1058 (Hager, 1984; McKenzie, 1967; Panasyuk and Hager, 2000; Richards and Hager, 1984; Steinberger et al.,
1059 2010). Based on recent crustal thickness and flexural modeling, Steinberger *et al* (2010) suggest that
1060 Earth's gravity anomalies with $\lambda_{1/2} \geq 650 \text{ km}$ ($l \leq 30$) are probably due to sources in the sublithospheric
1061 mantle, while those at shorter wavelengths have sources predominantly in the lithosphere. This downward

1062 revision of the upper limit for the diagnostic waveband therefore provides more room for the operation of
1063 the standard model, including mantle plumes.

1064

1065 Given the presence of a thermomechanical boundary layer at Earth's surface, some 700-km thick, as
1066 suggested by this study, the interpretation of gravity-topography spectra should be revisited. Based on
1067 earlier incipient modes analysis, a competent layer near the surface of a dynamic thermomechanical planet
1068 can be expected to develop low-amplitude material waves with wavelengths ranging from 2 to ζ times the
1069 layer thickness. Assuming the depths of the isobaric shears (Table 3) define a series of layer thicknesses,
1070 the equivalent ranges of angular degree can be worked out (Table 5). Coincidentally, the long-wavelength
1071 limit for folding of a layer M2 thick is $l = 22$, roughly coincident with the roll off in the gravity-topography
1072 correlation (Wieczorek, 2007). Furthermore, the empirical limit suggested by Steinberger *et al* (2010) is
1073 bracketed by the short-wavelength M4 and the long-wavelength M1 limits, and coincident with the short-
1074 wavelength M3 limit. In other words, the correlation they propose is supported by these findings, provided
1075 that the lithosphere is taken to include the continental tectosphere. However, the implications of
1076 thermomechanical theory for convection in the deep mantle are dramatically different from those of the
1077 standard model. For example, the long-wavelength M3 and M4 limits are $l = 8$ (Table 5). Consequently,
1078 gravity and geoid anomalies only with $\lambda_{1/2} > 2500 \text{ km}$ ($l < 8$) can be unequivocally associated with lower
1079 mantle convection. Coincidentally, this is the scale of robust lateral variations imaged by seismic
1080 tomography (Dziewonski et al., 1977; Dziewonski and Woodward, 1992; Gu et al., 2001). Furthermore,
1081 given the inverse temperature dependence of thermal expansivity for inhomogeneous elastic solids, any
1082 convection process in the lower mantle is likely to be rather sluggish. Detailed study of these intriguing
1083 spectral observations is in progress. Finally, material coupling in these layers is likely to have a measurable
1084 impact on the attenuation of intermediate and long-period surface waves, consistent with the predicted non-
1085 adiabaticity of the upper mantle (Durek and Ekstrom, 1996; Romanowicz, 1995).

1086

1087 **8.0 Conclusion**

1088 Global plate motions are the result of a complex planetary-scale rock mechanics experiment, where the
1089 motive force of gravity drives thermomechanically competent oceanic lithosphere into the relatively

EARTHQUAKE DEPTH-ENERGY RELEASE

1090 weaker rock units of the continents. Under extreme pressures, isobaric shearing at discrete depths
1091 facilitates toroidal plate motions, i.e., Euler rotations of spheroidal caps, while minimizing global energy
1092 dissipation. The fractal depth distribution of these disclinations is dictated by the statistically-stable
1093 thermomechanics of shear localization in inhomogeneous non-linear elastic self-gravitating solids, and
1094 scales with the thickness of mature oceanic lithosphere, where the greatest density contrasts and
1095 gravitational body forces reside. At low pressures, shear localization in crustal rocks occurs as dislocations
1096 at finite angles with respect to the shortening direction, with a 30 degree angle being the most likely.
1097 Consequently, relatively low-angle ($\sim 30^\circ$) reverse faults, steep ($\sim 60^\circ$) normal faults, and triple junctions
1098 with orthogonal or hexagonal symmetries are likely to form in regions of crustal shortening, extension, and
1099 transverse motion, respectively. In convergent plate boundary regions, this results in the overall thickening
1100 and seismogenic deformation of weaker rocks in the zone. Once convergence ceases, these regional high-
1101 potential energy welts relax over 30 Ma periods, often exposing equilibrium assemblages of middle- and
1102 lower-crustal rocks at the surface which are bounded by crustal scale shear zones. Deep crustal migmatites
1103 are produced by dehydration anatexis during shortening, and heat release following gravitational collapse
1104 drives further melting and differentiation of the crust. Equilibrium pressures in these crystalline cores are
1105 consistent with exhumation from 25- and 37-km depths, coincident with the L1 and L2 isobaric shears of
1106 ThERM. At extensional plate margins, brittle failure of crustal rocks depressurizes the subjacent mantle,
1107 resulting in its partial fusion and the subsequent eruption of basaltic lavas. These lavas cool and solidify,
1108 preserving a record of the ambient magnetic field. At transform margins, seismic energy dissipation is
1109 limited to about 25-km depth, but can be distributed over a wide region, depending on the competence of
1110 the rocks on either side of the fault. Wider shear zones are likely in continental regions, because of the
1111 lower competence of felsic crust. The dominance of toroidal motions at Earth's surface can be attributed to
1112 the combination of liquid water, which has a profound weakening effect on common rocks and minerals,
1113 and the localization of shear at discrete depths within the thermomechanical Earth. The absence of plate
1114 tectonics on other terrestrial planets is simply due to the small number of known examples. Furthermore,
1115 the correlation and admittance of Earth's gravity-topography spectra can be reconciled with this novel
1116 thermomechanical theory. In consequence, mantle convection, in the sense of the standard model, is
1117 possible only in the deep mantle at a scale $\lambda_{1/2} > 2500 \text{ km}$ ($l < 8$), consistent with the scale of robust lateral

1118 variations imaged by seismic tomography. Finally, the temperature dependence of thermal expansivity for
1119 this thermomechanical Earth makes vigorous convection in the lower mantle unlikely. The dominant mode
1120 of thermal convection for the planet, therefore, looks and acts like a dynamic version of plate tectonics.

1121

1122 **Acknowledgements.** The figures were prepared using the Generic Mapping Tools (Wessel and Smith,
1123 1998). I thank Professor A. John Watkinson for his unflagging support and quiet insistence that structural
1124 observations at all scales matter, Professor Bruce E. Hobbs for his support and leadership on matters
1125 thermodynamical, Professor Raymond Joesten for pointing out the coincidence of planar tectonite fabrics in
1126 mantle xenoliths from depths consistent with mode M1, and Professor Frank Horowitz for suggesting the
1127 least-squares fitting of ThERM to PREM. This paper is dedicated to the memory of Dr. Peter Hornby.

1128 REFERENCES

- 1129 Adams, L.H., Williamson, E.D., 1923. The composition of the Earth's interior.
 1130 Smithsonian Report, 241-260.
- 1131 Aki, K., Richards, P.G., 2002. Quantitative Seismology, 2nd ed. University Science
 1132 Books, Sausalito, CA.
- 1133 Amante, C., Eakins, W., 2009. ETOPO1 1 arc-minute global relief model: procedures,
 1134 data sources and analysis. NOAA, Boulder, p. 25.
- 1135 Anderson, D.L., 1989. Theory of the Earth. Blackwell Scientific Publications, Boston.
- 1136 Anderson, D.L., 2007. New Theory of the Earth. Cambridge University Press,
 1137 Cambridge.
- 1138 Artemieva, I.M., 2009. The continental lithosphere: Reconciling thermal, seismic, and
 1139 petrologic data. *Lithos* 109, 23-46.
- 1140 Artemieva, I.M., Billien, M., Leveque, J.-J., Mooney, W.D., 2004. Shear wave velocity,
 1141 seismic attenuation, and thermal structure of the continental upper mantle. *Geophysical*
 1142 *Journal International* 157, 607-628.
- 1143 Artemieva, I.M., Mooney, W.D., 2001. Thermal thickness and evolution of Precambrian
 1144 lithosphere: A global study. *Journal of Geophysical Research* 106, 16387-16414.
- 1145 Atwater, T., 1970. Implications of plate tectonics for the Cenozoic tectonic evolution of
 1146 western North America. *BGSA* 81, 3513-3536.
- 1147 Barrell, J., 1914. The strength of the Earth's crust. VI. Relations of isostatic movements
 1148 to a sphere of weakness - the asthenosphere. *Journal of Geology* 22, 655-683.
- 1149 Benioff, H., 1954. Orogenesis and deep crustal structure: additional evidence from
 1150 seismology. *Bulletin Geological Society America* 65, 385-400.
- 1151 Bercovici, D., Ricard, Y., Richards, M.A., 2000. The relation between mantle dynamics
 1152 and plate tectonics: a primer, in: Richards, M.A., Gordon, R.G., van der Hilst, R.D.
 1153 (Eds.), *The history and dynamics of global plate motions*. American Geophysical Union,
 1154 Washington D.C., pp. 5-46.
- 1155 Birch, F., 1952. Elasticity and constitution of Earth's interior. *Journal of Geophysical*
 1156 *Research* 57, 227-286.
- 1157 Boyd, F.R., 1973. A pyroxene geotherm. *Geochimica et Cosmochimica Acta* 37, 2533-
 1158 2546.
- 1159 Brown, M., 2007. Metamorphic conditions in orogenic belts: A record of secular change.
 1160 *International Geology Review* 49, 193-234.
- 1161 Brown, M., 2008. Characteristic thermal regimes of plate tectonics and their
 1162 metamorphic imprint throughout Earth history: when did Earth first adopt a plate
 1163 tectonics mode of behavior? *GSA Special Publication* 440, 97-128.
- 1164 Bunge, H.-P., Richards, M.A., Baumgardner, J.R., 1997. A sensitivity study of three-
 1165 dimensional spherical mantle convection at 10^8 Rayleigh number: effects of depth-
 1166 dependent viscosity, heating mode, and an endothermic phase change. *Journal of*
 1167 *Geophysical Research* 102, 11991-12007.
- 1168 Chandrasekhar, S., 1967. *An Introduction to the Study of Stellar Structure*. Dover
 1169 Publications, Mineola, NY.
- 1170 Chao, B.F., Gross, R.S., 1995. Changes in the Earth's rotational energy induced by
 1171 earthquakes. *Geophysical Journal International* 122, 776-783.
- 1172 Chao, B.F., Gross, R.S., Dong, D.-N., 1995. Changes in global gravitational energy
 1173 induced by earthquakes. *Geophysical Journal International* 122, 784-789.

- 1174 Clauser, C., Huenges, E., 1995. Thermal conductivity of rocks and minerals, AGU
 1175 Reference Shelf 3: A Handbook of Physical Constants - Rock Physics and Phase
 1176 Relations AGU, Washington D.C., pp. 105-125.
- 1177 Crosby, A.G., McKenzie, D.P., Sclater, J.G., 2006. The relationship between depth, age
 1178 and gravity in the oceans. *Geophysical Journal International* 166, 553-573.
- 1179 Dewey, J.F., Bird, J.M., 1970. Mountain belts and the new global tectonics. *Journal of*
 1180 *Geophysical Research* 75, 2625-2647.
- 1181 Dietz, R.S., 1961. Continent and ocean basin evolution by spreading of the sea floor.
 1182 *Nature* 190, 854-857.
- 1183 Durek, J.J., Ekstrom, G., 1996. A radial model of anelasticity consistent with long-period
 1184 surface-wave attenuation. *Bulletin of the Seismological Society of America* 86, 144-158.
- 1185 Dziewonski, A.M., Anderson, D.L., 1981. Preliminary reference Earth model. *Physics of*
 1186 *the Earth and Planetary Interiors* 25, 297-356.
- 1187 Dziewonski, A.M., Chou, T.-A., Woodhouse, J.H., 1981. Determination of earthquake
 1188 source parameters from waveform data for studies of global and regional seismicity.
 1189 *Journal of Geophysical Research* 86, 2825-2852.
- 1190 Dziewonski, A.M., Hager, B.H., O'Connell, R.J., 1977. Large-scale heterogeneities in the
 1191 lower mantle. *Journal of Geophysical Research* 82, 239-255.
- 1192 Dziewonski, A.M., Woodhouse, J.H., 1983. An experiment in systematic study of global
 1193 seismicity: centroid-moment tensor solutions for 201 moderate and large earthquakes of
 1194 1981. *Journal of Geophysical Research* 88, 3247-3271.
- 1195 Dziewonski, A.M., Woodward, R.L., 1992. Acoustic imaging at the planetary scale, in:
 1196 Emert, H., Harjes, H.-P. (Eds.), *Acoustical Imaging*. Plenum, New York, pp. 785-797.
- 1197 Einstein, A., 1916. *Die Grundlage der allgemeinen Relativitätstheorie*, in: Hawking, S.
 1198 (Ed.), *A Stubbornly Persistent Illusion: The Essential Scientific Writings of Albert*
 1199 *Einstein*. Running Press, Philadelphia, pp. 46-98.
- 1200 Ekstrom, G., Nettles, M., 2011. The Global Centroid-Moment-Tensor (CMT) Project.
 1201 Lamont Doherty Earth Observatory-Columbia University.
- 1202 Ekstrom, G., Nettles, M., Dziewonski, A.M., 2012. The global CMT project 2004-2010:
 1203 Centroid-moment tensors for 13017 earthquakes. *Physics of the Earth and Planetary*
 1204 *Interiors* 200, 1-9.
- 1205 Engdahl, E.R., Van der Hilst, R.D., Buland, R., 1998. Global teleseismic earthquake
 1206 relocation with improved travel times and procedures for depth determination. *Bulletin of*
 1207 *the Seismological Society of America* 88, 722-743.
- 1208 Frohlich, C., 1989. The nature of deep-focus earthquakes. *Annual Reviews of Earth and*
 1209 *Planetary Science* 17, 227-254.
- 1210 Green, H.W., 2005. New Light on Deep Earthquakes. *Scientific American*, 1-9.
- 1211 Gu, Y.J., Dziewonski, A.M., Su, W., Ekstrom, G., 2001. Models of mantle shear velocity
 1212 and discontinuities in the pattern of lateral heterogeneities. *Journal of Geophysical*
 1213 *Research* 106, 11169-11199.
- 1214 Hager, B.H., 1984. Subducted slabs and the geoid: constraints on mantle rheology and
 1215 flow. *Journal of Geophysical Research* 89, 6003-6015.
- 1216 Hess, H.H., 1962. History of the ocean basins, in: Engel, A.E.J., James, H.L., Leonard,
 1217 B.F. (Eds.), *Petrological Studies: A Volume in Honor of A.F. Buddington*. Geological
 1218 Society of America, Boulder, CO, pp. 599-620.

- 1219 Hill, R.E.T., Hutchinson, J.W., 1975. Bifurcation Phenomena in the Plane Tension Test.
 1220 Journal of the Mechanics and Physics of Solids 23, 239-264.
- 1221 Hobbs, B.E., Ord, A., Regenauer-Lieb, K., 2011. The thermodynamics of deformed
 1222 metamorphic rocks: A review. Journal of Structural Geology 33, 758-818.
- 1223 Isacks, B., Oliver, J., Sykes, L.R., 1968. Seismology and the new global tectonics.
 1224 Journal of Geophysical Research 73, 5855-5899.
- 1225 Jackson, I., Webb, S., Weston, L., Boness, D., 2005. Frequency dependence of elastic
 1226 wave speeds at high temperature: a direct experimental demonstration. Physics of the
 1227 Earth and Planetary Interiors 148, 85-96.
- 1228 James, D.E., Boyd, F.R., Schutt, D.L., Bell, D.R., Carlson, R.W., 2004. Xenolith
 1229 constraints on seismic velocities in the upper mantle beneath southern Africa.
 1230 Geochemistry Geophysics Geosystems 5, 1-32.
- 1231 Jordan, T.H., 1975. The continental tectosphere. Reviews of Geophysics and Space
 1232 Physics 13, 1-12.
- 1233 Jordan, T.H.C., Beroza, G., Cornell, C.A., Crouse, C.B., Dieterich, J., Frankel, A.,
 1234 Jackson, D.D., Johnston, A., Kanamori, H., Langer, J.S., McNutt, M.K., Rice, J.,
 1235 Romanowicz, B.A., Sieh, K., Somerville, P.G., 2003. Living on an Active Earth:
 1236 Perspectives on Earthquake Science. The National Academies Press, Washington, D.C.
- 1237 Karato, S., 1993. Importance of Anelasticity in the Interpretation of Seismic
 1238 Tomography. Geophysical Research Letters 20, 1623-1626.
- 1239 Katz, O., Reches, Z., 2002. Pre-failure damage, time-dependent creep and strength
 1240 variations of a brittle granite, 5th International Conference on Analysis of Discontinuous
 1241 Deformation. Balkema, Rotterdam, Ben-Gurion University, Israel, pp. 1-5.
- 1242 Katz, O., Reches, Z., 2004. Microfracturing, damage and failure of brittle granites.
 1243 Journal of Geophysical Research 109, 10.1029/2002JB001961.
- 1244 Kaula, W.M., 1972. Global gravity and tectonics, in: Robertson, E.C., Hays, J.F.,
 1245 Knopoff, L. (Eds.), The Nature of the Solid Earth. McGraw-Hill, New York, pp. 385-405.
- 1246 Kennett, B.L.N., Engdahl, E.R., 1991. Travel times for global earthquake location and
 1247 phase identification. Geophysical Journal International 105, 429-465.
- 1248 Lavenda, B.H., 1995. Thermodynamics of Extremes. Albion Publishing, Chichester.
- 1249 Le Pichon, X., 1968. Sea-floor spreading and continental drift. Journal of Geophysical
 1250 Research 73, 3661-3697.
- 1251 Luh, P.C., 1975. Free oscillations of the laterally inhomogeneous Earth: Quasi-
 1252 degenerate multiplet coupling. Geophysical Journal of the Royal Astronomical Society
 1253 32, 203-218.
- 1254 Madariaga, R., 1972. Torsional free oscillations of the laterally heterogeneous Earth.
 1255 Geophysical Journal of the Royal Astronomical Society 27, 81-100.
- 1256 McKenzie, D.P., 1967. Some remarks on heat flow and gravity anomalies. Journal of
 1257 Geophysical Research 72, 6261-6273.
- 1258 McKenzie, D.P., 1969. Speculations on the consequences and causes of plate motions.
 1259 Geophysical Journal of the Royal Astronomical Society 18, 1-32.
- 1260 McKenzie, D.P., Morgan, W.J., 1969. Evolution of triple junctions. Nature 224, 125-133.
- 1261 McKenzie, D.P., Parker, R.D., 1967. The north Pacific: An example of tectonics on a
 1262 sphere. Nature 216, 1276-1280.
- 1263 Moores, E.M., Twiss, R.J., 1995. Tectonics. W. H. Freeman and Company, New York.

- 1264 Morgan, W.J., 1968. Rises, trenches, great faults, and crustal blocks. *Journal of*
 1265 *Geophysical Research* 73, 1958-1982.
- 1266 Needleman, A., 1979. Non-Normality and Bifurcation in Plane Strain Tension and
 1267 Compression. *Journal of the Mechanics and Physics of Solids* 27, 231-254.
- 1268 Panasyuk, S.V., Hager, B.H., 2000. Models of isostatic and dynamic topography, geoid
 1269 anomalies, and their uncertainties. *Journal of Geophysical Research* 105, 28199-28209.
- 1270 Parsons, B., Sclater, J.G., 1977. An analysis of the variation of ocean floor bathymetry
 1271 and heat flow with age. *Journal of Geophysical Research* 82, 803-827.
- 1272 Patton, R.L., 1997. On the general applicability of relaxation modes in continuum models
 1273 of crustal deformation, Department of Geology. Washington State University, Pullman,
 1274 p. 129.
- 1275 Patton, R.L., 2001. Earth's potentiophere. EOS Transactions AGU Fall Meeting
 1276 Supplement 82, T41B-0860.
- 1277 Patton, R.L., 2005. Non-linear viscoelastic models of rock folding and faulting, in:
 1278 Hancock, H., Fisher, L., Baker, T., Bell, T., Blenkinsop, T.G., Chapman, L., Cleverley,
 1279 J.S., Collins, B., Duckworth, R., Ewins, P., Ford, P., Oliver, A., Oliver, N., Rubenach, M.,
 1280 Williams, P. (Eds.), STOMP: Structure, Tectonics and Ore Mineralization Processes.
 1281 James Cook, Townsville, QLD, Australia, p. 103.
- 1282 Patton, R.L., Manoranjan, V.S., Watkinson, A.J., 2000. Plate formation at the surface of a
 1283 convecting fluid, XIIIth International Congress on Rheology. The British Society of
 1284 Rheology, Cambridge, U.K., pp. 167-169.
- 1285 Patton, R.L., Watkinson, A.J., 2005. A viscoelastic strain energy principle expressed in
 1286 fold-thrust belts and other compressional regimes. *Journal of Structural Geology* 27,
 1287 1143-1154.
- 1288 Patton, R.L., Watkinson, A.J., 2009. Thermomechanical Earth Reference Model. EOS
 1289 Transactions AGU Fall Meeting Supplement 90, NG43B-1228.
- 1290 Patton, R.L., Watkinson, A.J., 2010. Shear localization in solids: insights for mountain
 1291 building processes from a frame-indifferent ideal material model, in: Law, R.D., Butler,
 1292 R.W.H., Holdsworth, R.E., Krabbendam, M., Strachan, R.A. (Eds.), *Continental*
 1293 *Tectonics and Mountain Building: the Legacy of Peach and Horne*. Geological Society,
 1294 London, pp. 739-766.
- 1295 Patton, R.L., Watkinson, A.J., 2011. Deformation localization in orogens: spatiotemporal
 1296 and thermodynamic constraints, in: Druguet, E., Carreras, J., Alsop, G.I., Bons, P.D.,
 1297 Czeck, D.M., Hudleston, P.J., Siddoway, C.S. (Eds.), *Deformation Localization in Rocks:*
 1298 *New Advances (keynote)*. Penrose Conferences, Geological Society of America,
 1299 Cadaques and Cap de Creus, Catalonia, Spain.
- 1300 Patton, R.L., Watkinson, A.J., in review. Deformation localization in orogens:
 1301 spatiotemporal expression and thermodynamic constraint. *Journal of Structural Geology*
 1302 SG-D-11_00259R1.
- 1303 Presnall, D.C., Gudfinnsson, G.H., 2008. Origin of the oceanic lithosphere. *Journal of*
 1304 *Petrology* 49, 615-632.
- 1305 Richards, M.A., Hager, B.H., 1984. Geoid anomalies in a dynamic Earth. *Journal of*
 1306 *Geophysical Research* 89, 5987-6002.
- 1307 Ringwood, A.E., 1991. Phase transformations and their bearing on the constitution and
 1308 dynamics of the mantle. *Geochimica et Cosmochimica Acta* 55, 2083-2110.

EARTHQUAKE DEPTH-ENERGY RELEASE

- 1309 Romanowicz, 1994. Anelastic tomography: a new perspective on upper mantle thermal
1310 structure. *Earth and Planetary Science Letters* 128, 113-121.
- 1311 Romanowicz, B., 1995. A global tomographic model of shear attenuation in the upper
1312 mantle. *Journal of Geophysical Research* 100, 12375-12394.
- 1313 Rudnick, R.L., Gao, S.S., 2003. *Composition of the Continental Crust*, Treatise on
1314 Geochemistry. Elsevier, pp. 1-64.
- 1315 Steinberger, B., Werner, S.C., Torsvik, T.H., 2010. Deep versus shallow origin of gravity
1316 anomalies, topography and volcanism on Earth, Venus and Mars. *Icarus* 207, 564-577.
- 1317 Tackley, P.J., 2000. The quest for self-consistent generation of tectonic plates in mantle
1318 convection models, in: Richards, M.A., Gordon, R.G., van der Hilst, R.D. (Eds.), *The*
1319 *history and dynamics of global plate motions*. American Geophysical Union,
1320 Washington, D.C., pp. 47-72.
- 1321 Truesdell, C., 1964. The natural time of a viscoelastic fluid: Its significance and
1322 measurement. *Physics of Fluids* 7, 1134-1142.
- 1323 Turcotte, D.L., Oxburgh, E.R., 1967. Finite amplitude convective cells and continental
1324 drift. *Journal of Fluid Mechanics* 28, 29-42.
- 1325 Vine, F.J., Matthews, D.H., 1963. Magnetic anomalies over oceanic ridges. *Nature* 199,
1326 947-949.
- 1327 Vosteen, H.-D., Schellschmidt, R., 2003. Influence of temperature on thermal
1328 conductivity, thermal capacity and thermal diffusivity for different types of rock. *Physics*
1329 *and Chemistry of the Earth* 28, 499-509.
- 1330 Watts, A.B., 2001. *Isostasy and Flexure of the Lithosphere*. Cambridge University Press,
1331 Cambridge.
- 1332 Wegener, A., 1966. *The origin of continents and oceans*, 4th ed. Dover, New York.
- 1333 Wessel, P., Smith, W.H.F., 1998. New improved version of the Generic Mapping Tools
1334 released. *EOS Transactions American Geophysical Union* 76, 579.
- 1335 Widmer, R., Masters, G., Gilbert, F., 1991. Spherically symmetric attenuation within the
1336 Earth from normal mode data. *Geophysical Journal International* 104, 541-553.
- 1337 Wieczorek, M.A., 2007. Gravity and topography of the terrestrial planets, in: Schubert,
1338 G. (Ed.), *Treatise on Geophysics*. Elsevier.
- 1339 Wilson, J.T., 1965. A new class of faults and their bearing on continental drift. *Nature*
1340 207, 343-347.
- 1341
- 1342

Figure captions

Figure 1. Plots of a) hypocenter and b) centroid depths for the 20646 algorithmically relocated earthquakes from the global CMT catalog (Ekstrom and Nettles, 2011), with origin times in the period January 1976 through December 2010. With increasing depth, the color breaks coincide with the isobaric shears H4, L1, L2, L4, M1, M2, and M4, of the ThERM (Patton and Watkinson, 2009, 2010). The CMT relocation procedure generally maps crustal seismicity to deeper levels, as indicated by the contrasting orange and yellow hues of ocean ridge earthquakes.

Figure 2. Plots of centroid depths for earthquakes in six tectonic settings (Table 4):

a) continental transform; b) Himalaya-type convergence; c) oceanic ridge/transform; d) island arc-type convergence; e) continental rift; and f) Andean-type convergence.

These subsets of the CMT catalog are used to compute the earthquake depth-energy release curves appearing in Figures 3-5.

Figure 3. Plots of seismic depth-energy release $\Sigma M_W(z;3)$, smoothed using a 3-km thick boxcar filter and color-keyed by tectonic setting (Table 4, Figure 2): a) Hypocenter depth-release curves exhibit sharp peaks at about 10- and 30-km depths and appear somewhat artificial, most likely due to the quick-epicenter location routines used by the USGS and ISC; b) Centroid depth-release curves span a broad range of depths and exhibit peak energy release at 17- to 18-km depths. The peak amplitude of most curves is proportional to the number of earthquakes in that tectonic setting. About $\frac{3}{4}$ of the earthquakes in this catalog occur in island arc-type convergence zones.

Figure 4. Plots of seismic depth-energy release $\Sigma M_W(z;3)/N$, smoothed using a 3-km thick boxcar filter, normalized by the number of events N , and color-keyed by tectonic setting (Table 4, Figure 2): a) depth-release curves at divergent and transform margins extend no deeper than about 50 km, and exhibit large positive and negative excursions from the global average at typical crustal levels. The deepest earthquakes coincide with the MORB source region (Presnall and Gudfinnsson, 2008); b) depth-release

curves at convergent margins extend to depths of about 700 km, and also exhibit large positive and negative excursions from the global average at typical crustal levels.

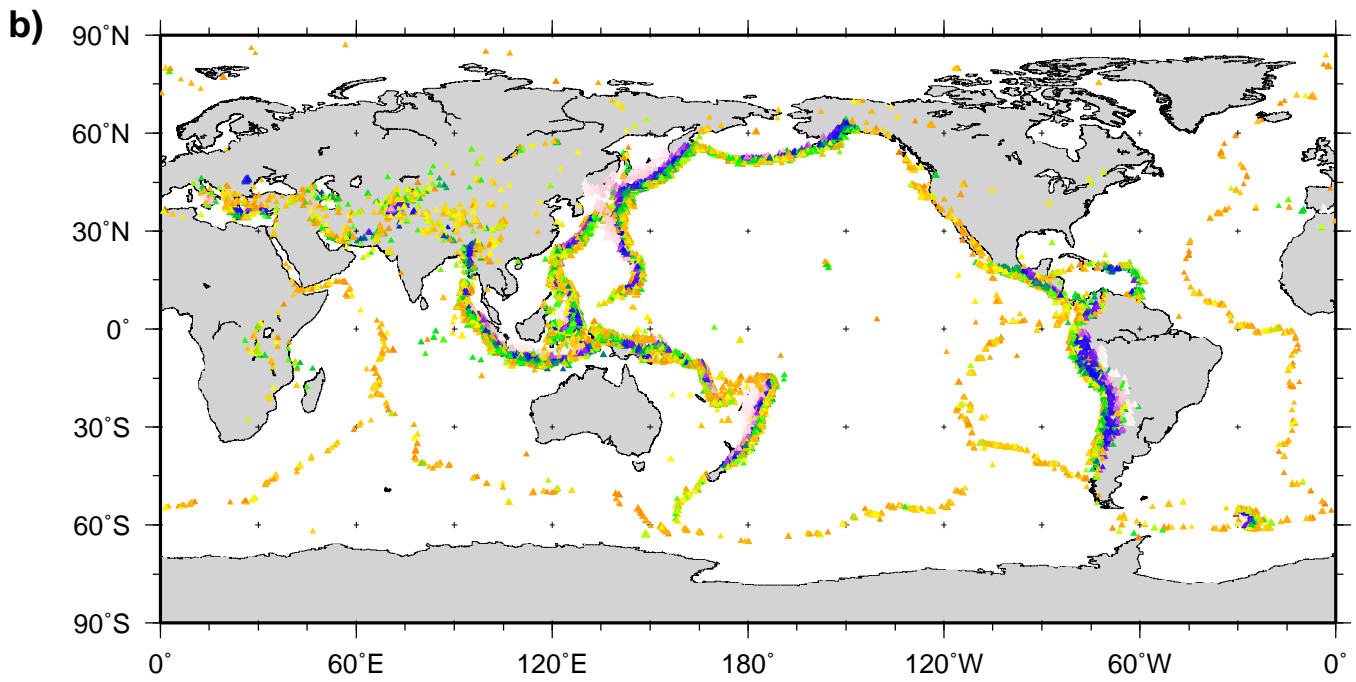
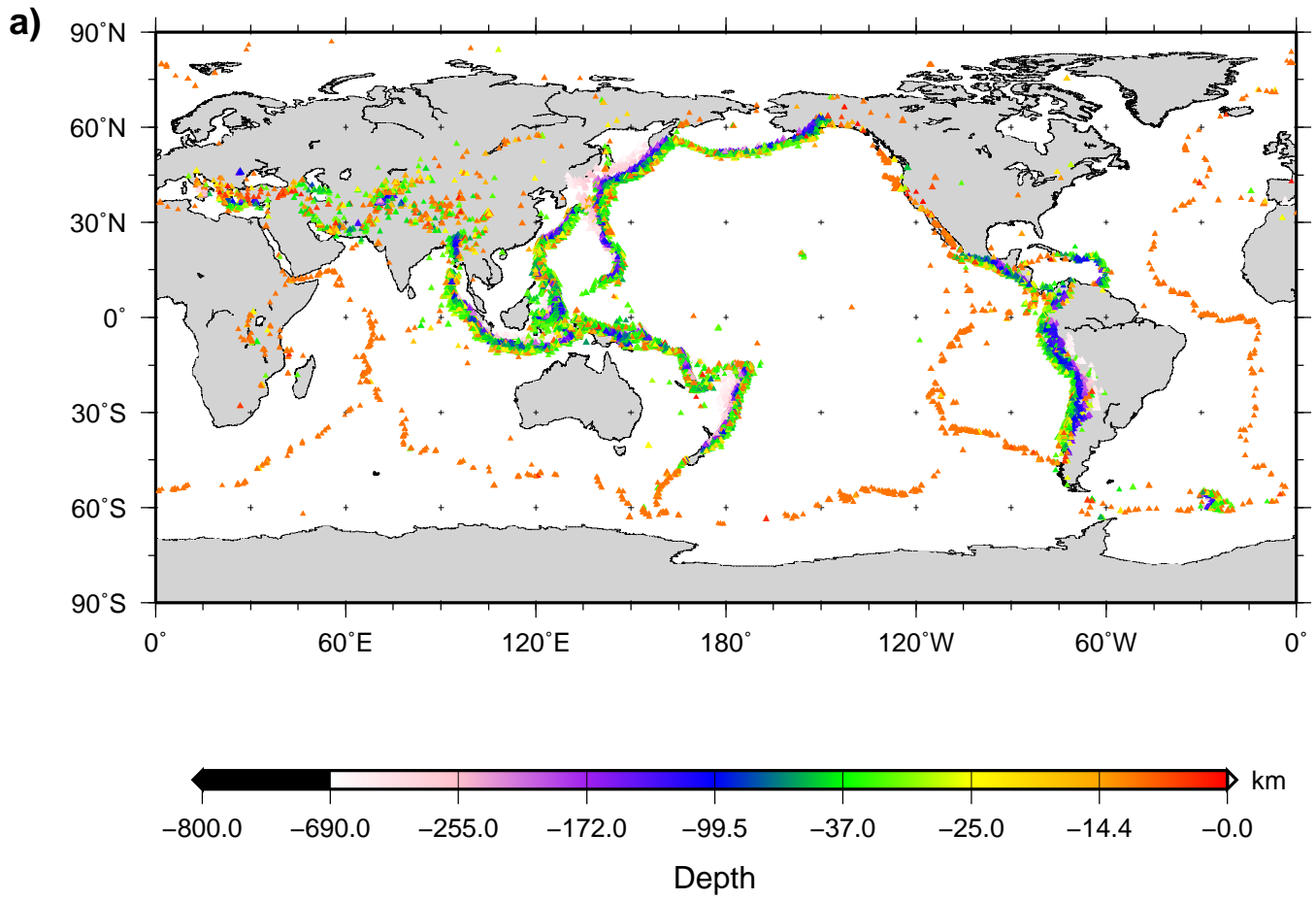
Figure 5. Color-keyed plots of seismic energy release with depth $\Sigma M_w(z;10)/N$, normalized by the number of events N in convergent margins, and smoothed with a boxcar filter 10-km thick. While the seismic energy release with depth in island arc-type convergent margins (purple) closely approximates the global baseline (black dashed), the Himalaya-type (green) and Andean-type (blue) margins display marked deviations in depth ranges. Positive and negative excursions of these curves likely indicate lateral variations mantle strength, and suggest stratification consistent with modes L4, M1, and M2 of ThERM (Patton and Watkinson, 2009).

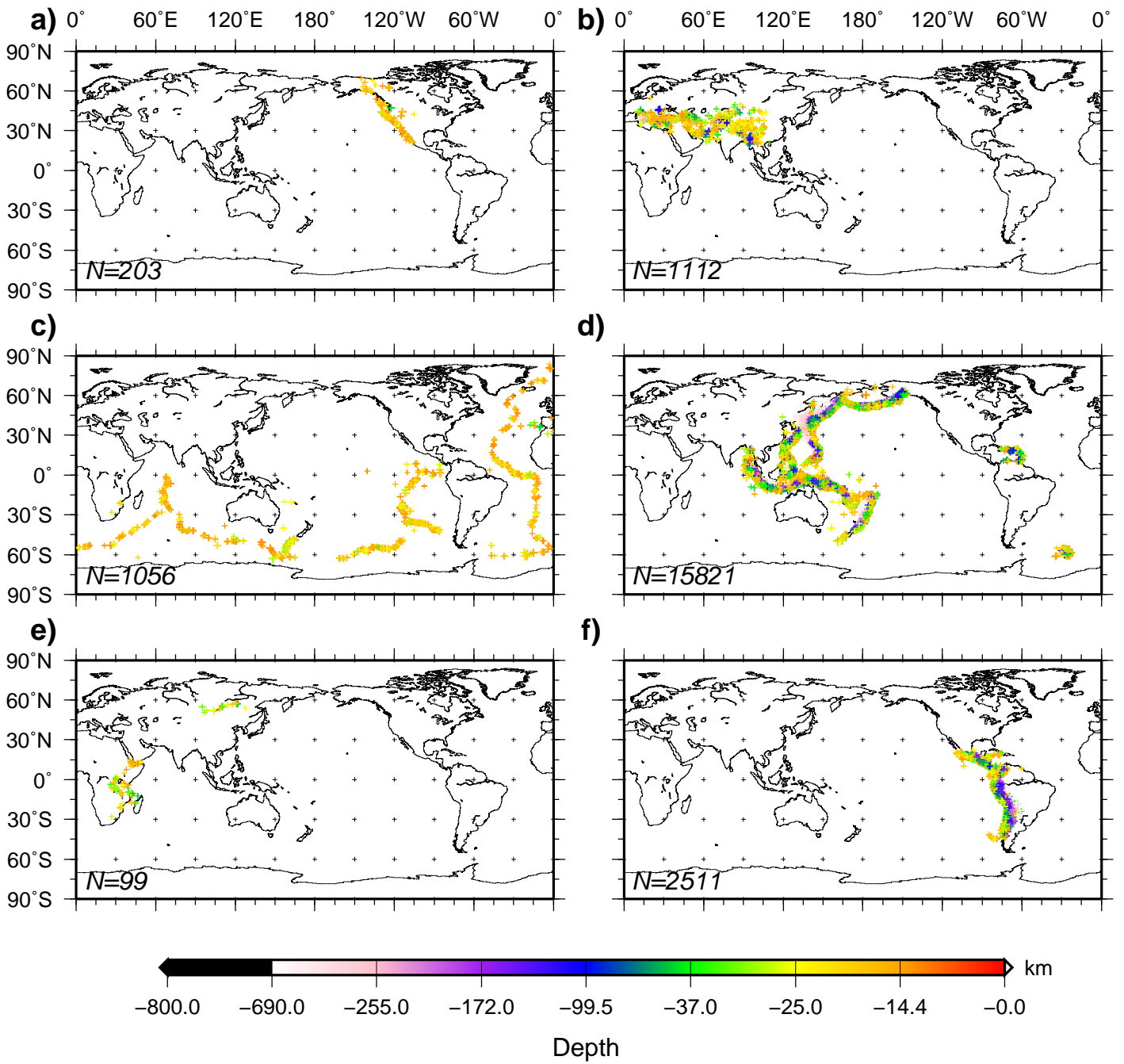
Figure 6. Graphical summary of the statistical thermodynamics of strained inhomogeneous elastic and self-gravitating matter configurations: a) mechanical variability bears little insight for DG-2 materials; b) statistical variability offers crucial insight for the thermodynamics of shear localization in DG-2 materials

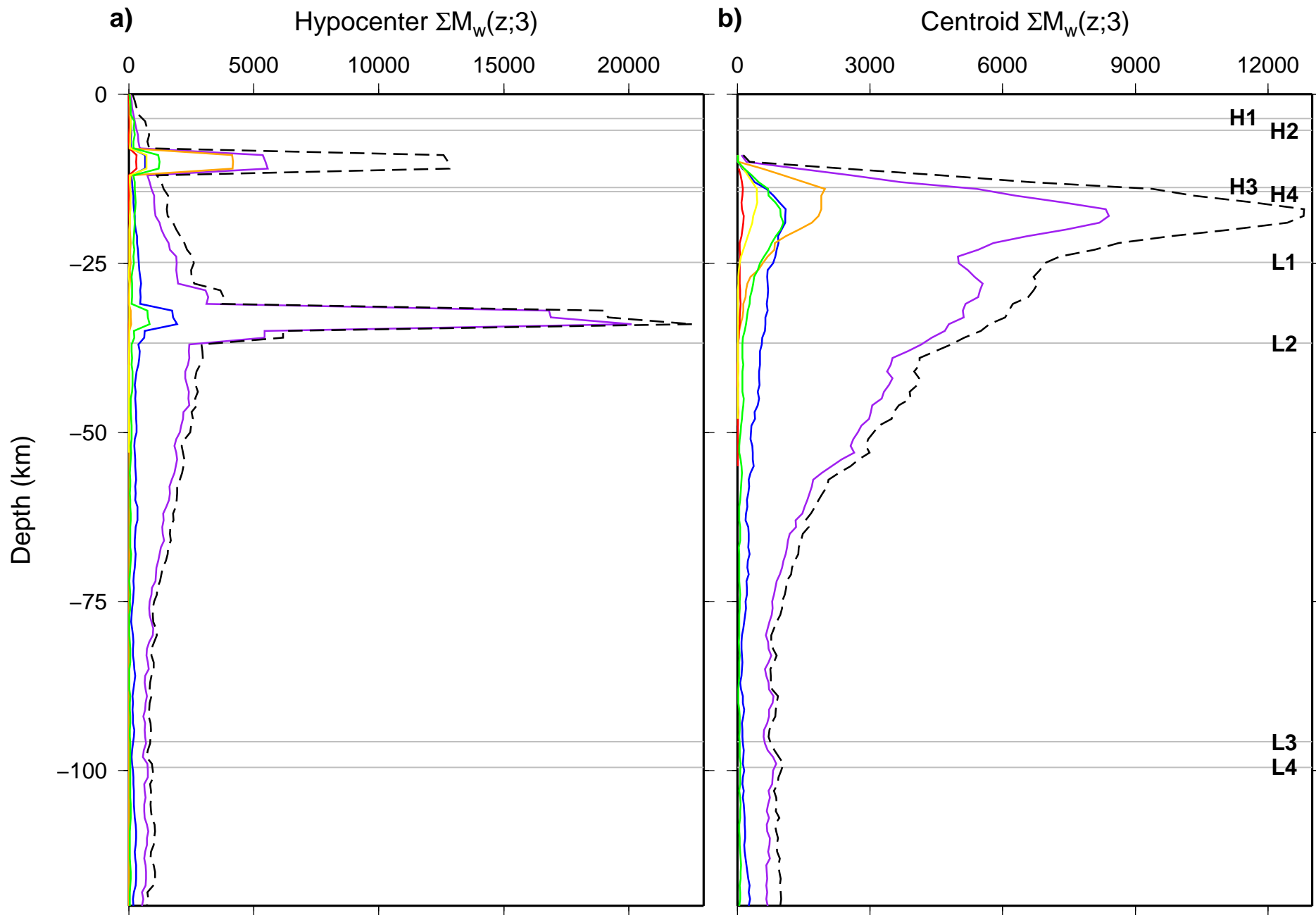
Figure 7. Correlation of experimental data from fourteen samples of the Mt. Scott granite, subjected to load-hold analysis (Katz and Reches, 2002, 2004), with the predictions of statistical thermodynamics and deformation modes of DG-2 materials: a) Normalized differential stresses (NDS) on intact samples ($\psi = \zeta$ NDS) are plotted as functions of diameter/length (d/l) for load-hold (green circles, red diamonds) and load-to-failure tests (orange diamonds). Three samples (red diamonds) spontaneously failed during the designated hold period. All macroscopically failed samples (diamonds) plot above the localization threshold curve (ψ^L , orange) given the range of standard error in Coulomb strength for the Mt. Scott granite (586 ± 16 MPa, dashed curves, inset); b) Populations of microscopic cracks with respect to the loading direction, observed post-loading, fall in the range $1/2 < \kappa/\chi < 2.9$, while macroscopic shears fall in the range $0.6 < \kappa/\chi < 0.9$. The thermomechanically rigid portion of this system is the stiff load frame itself, which by definition plots at $\kappa/\chi = 1$. The wide range of microscopic crack angles probably reflects the prior geometry of sample grain-size and fabric.

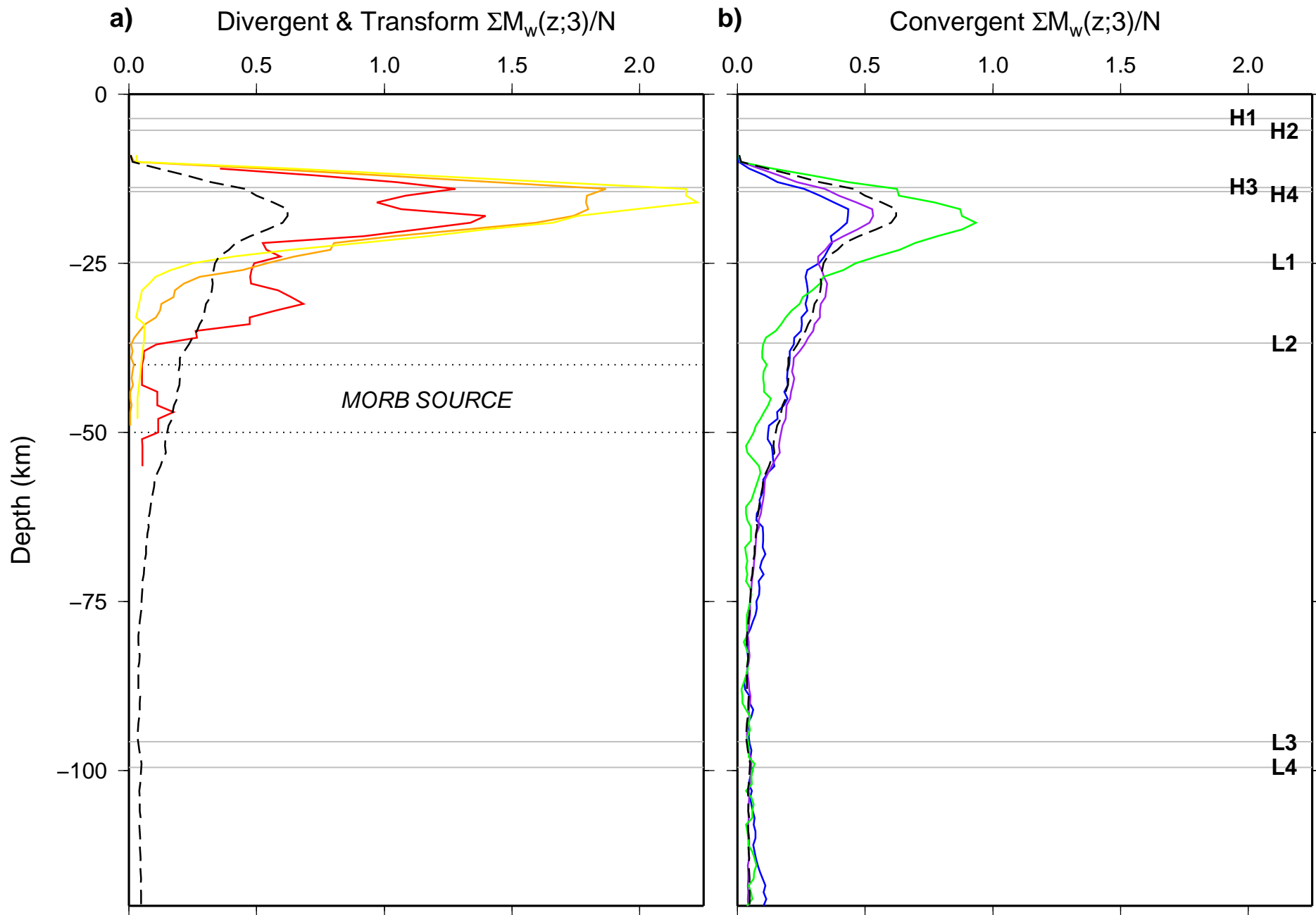
Figure 8. Comparison of ThERM (Patton and Watkinson, 2009), scaled to a fundamental thickness of 99.54 km representing mature oceanic lithosphere, with depth variations in compressional V_p and shear V_s wave speeds, density ρ (Dziewonski and Anderson, 1981), and normalized seismic depth-energy release $\Sigma M_w(z)/N$ (Figure 4b). The thickness of cratons and shields (Artemieva and Mooney, 2001) correlate with the M1 and M2 shears of ThERM (Patton and Watkinson, 2009), while the depth cut-off of seismicity, at about 700-km depth (Frohlich, 1989), correlates with M3-4. Given that thermomechanical competence generally decreases with depth in ThERM, subducting slabs are likely to freely enter the lower mantle, in contrast to the mesosphere hypothesis (Isacks and Molnar, 1969; Isacks et al., 1968). The re-orientation of pressure and tension axes in deep earthquake focal mechanisms are therefore likely to result from anti-crack shear ruptures in metastable spinel mineral species at very high pressures (Green and Burnley, 1989). The depth cut-off of seismicity might result from a rapid decrease in entropy density at 700-km depth (Patton and Watkinson, in review).

Figure 9. Comparison of the crustal ‘overtones’ of ThERM (Patton and Watkinson, 2009), scaled to a thickness of $F\zeta^{-1} = 14.4 \text{ km}$ representing the brittle crust, with depth variations in compressional V_p and shear V_s wave speeds, density ρ (Dziewonski and Anderson, 1981), and normalized seismic depth-energy release $\Sigma M_w(z)/N$ (Figure 4). The greatest variations of earthquake depth-energy release correlate with the low-velocity zone, as well as several distinct levels in the crust, lithosphere, and tectosphere. In regions where the tectosphere is absent, the asthenosphere resides subjacent to the crust.

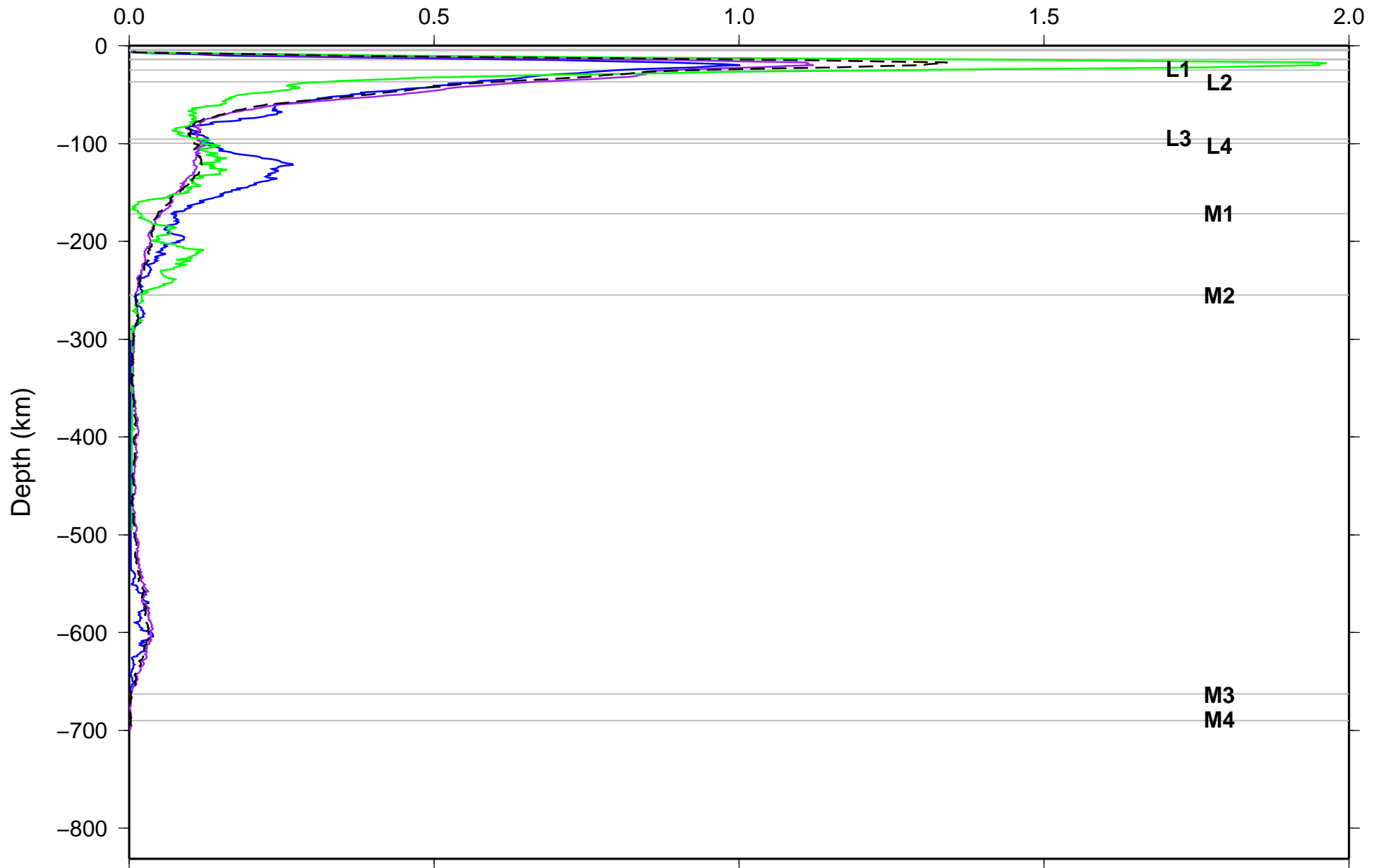




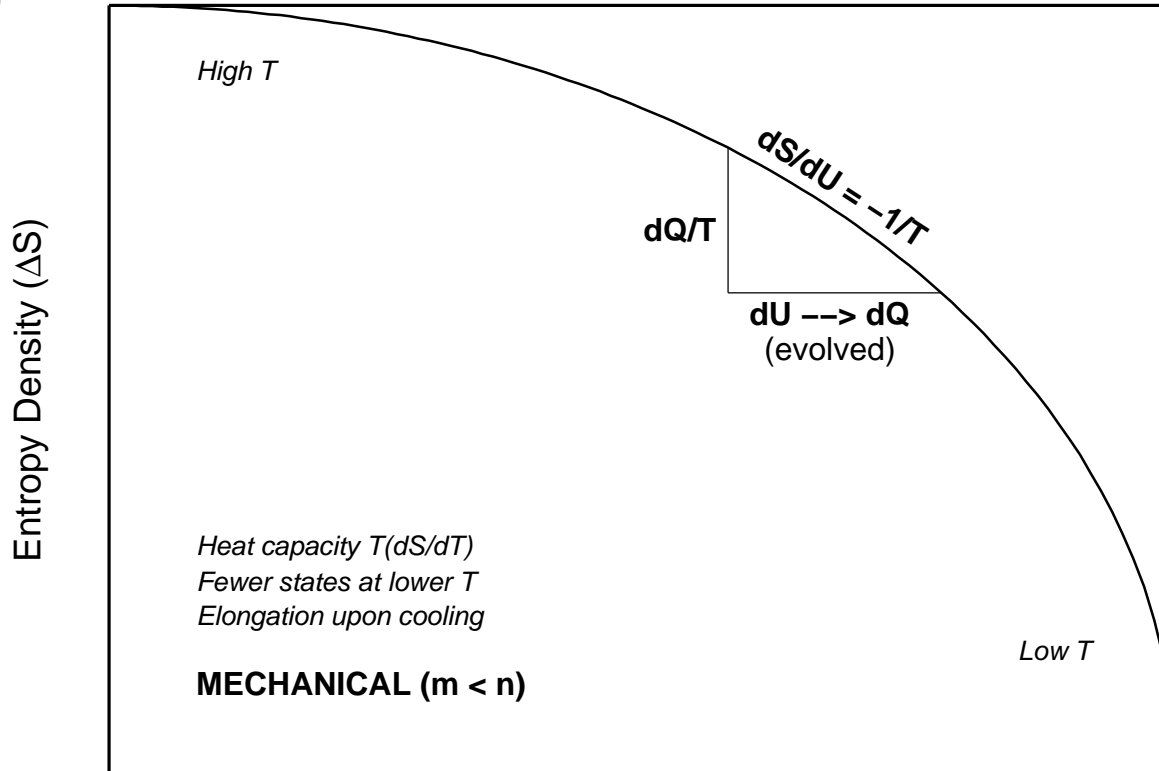




Convergent $\Sigma M_w(z;10)/N$

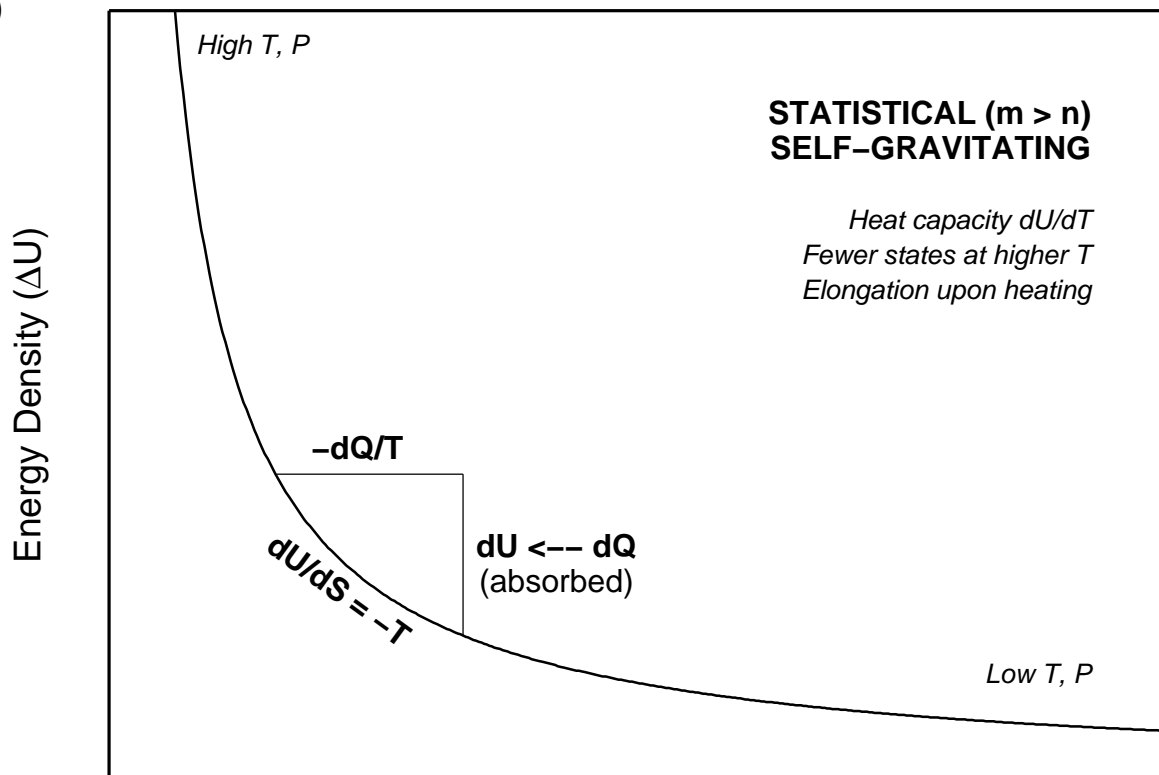


a)

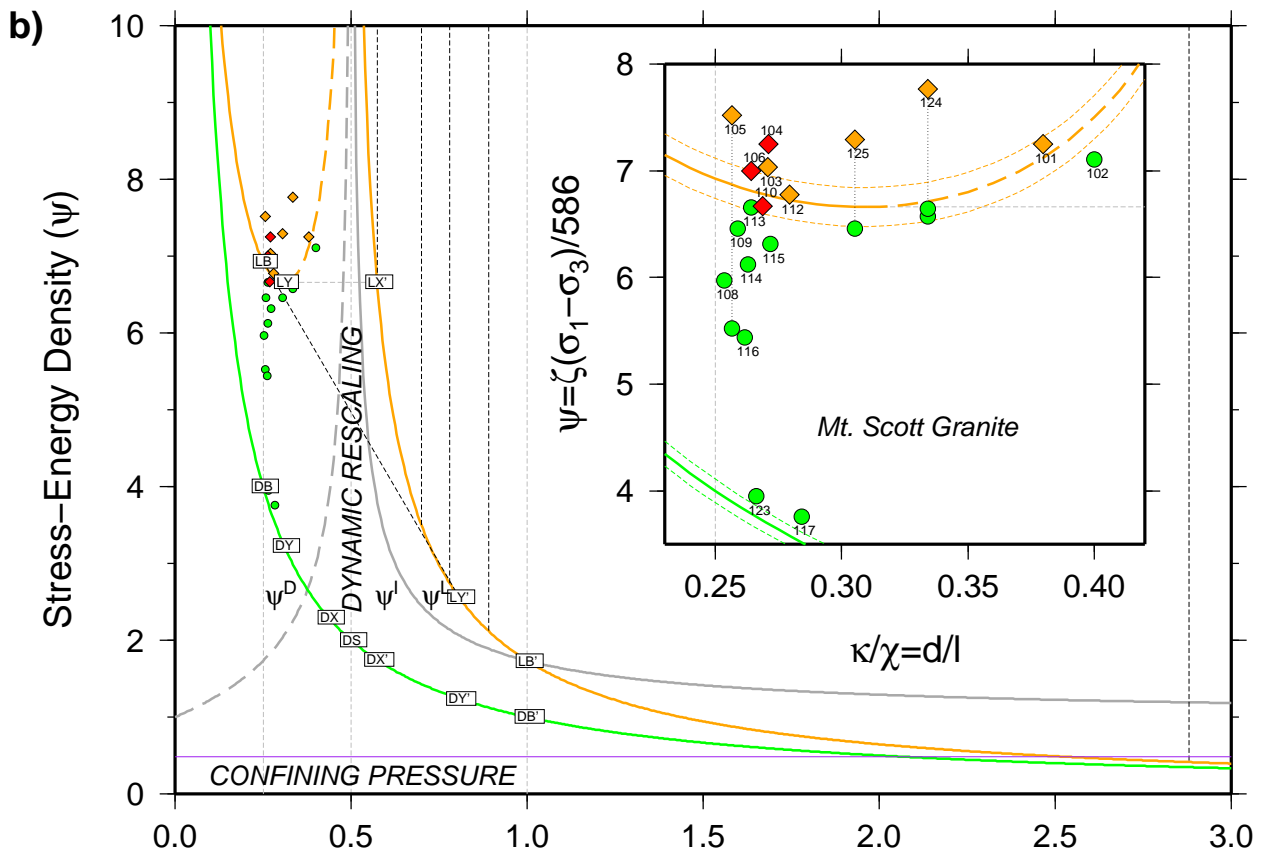
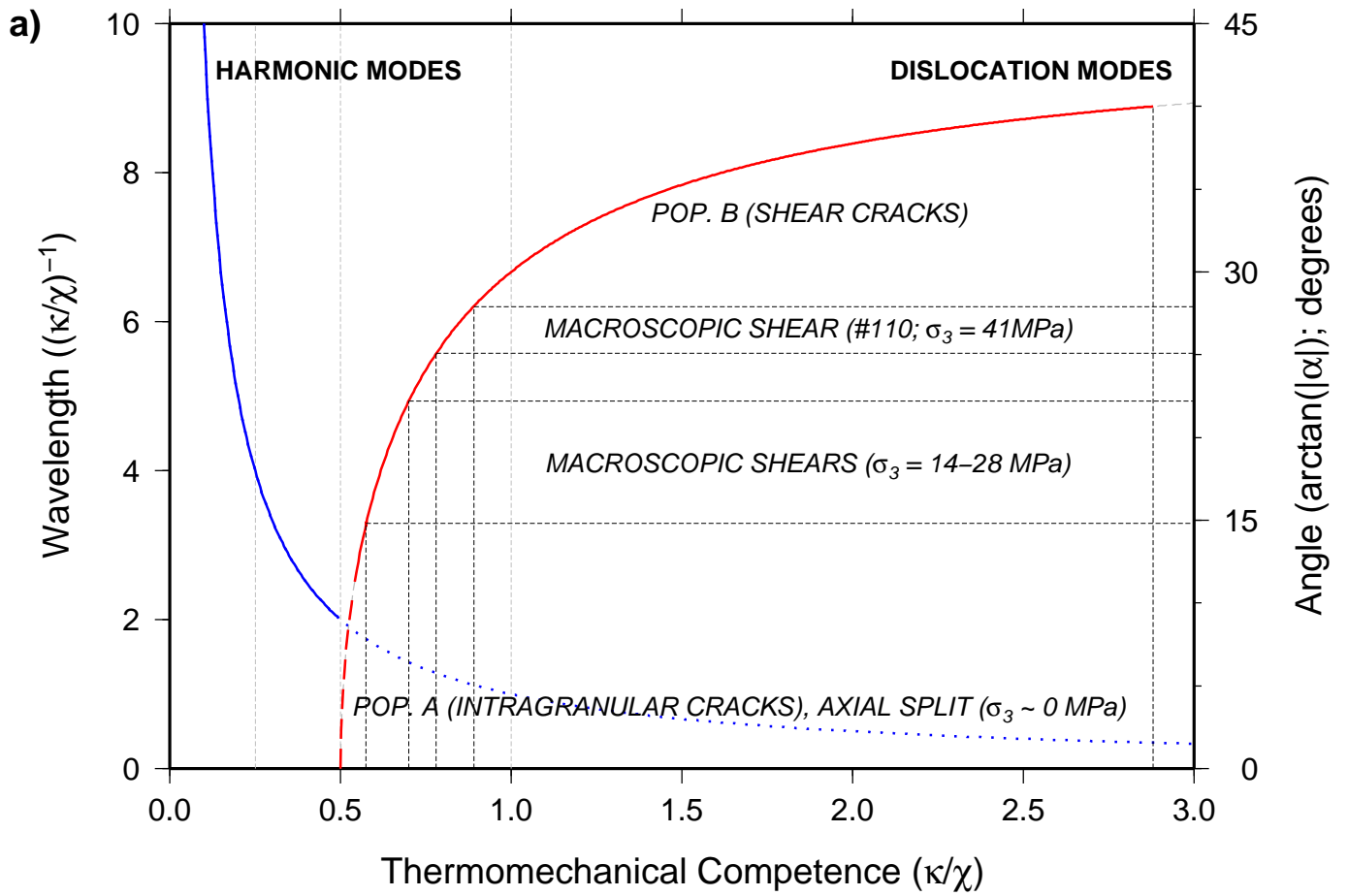


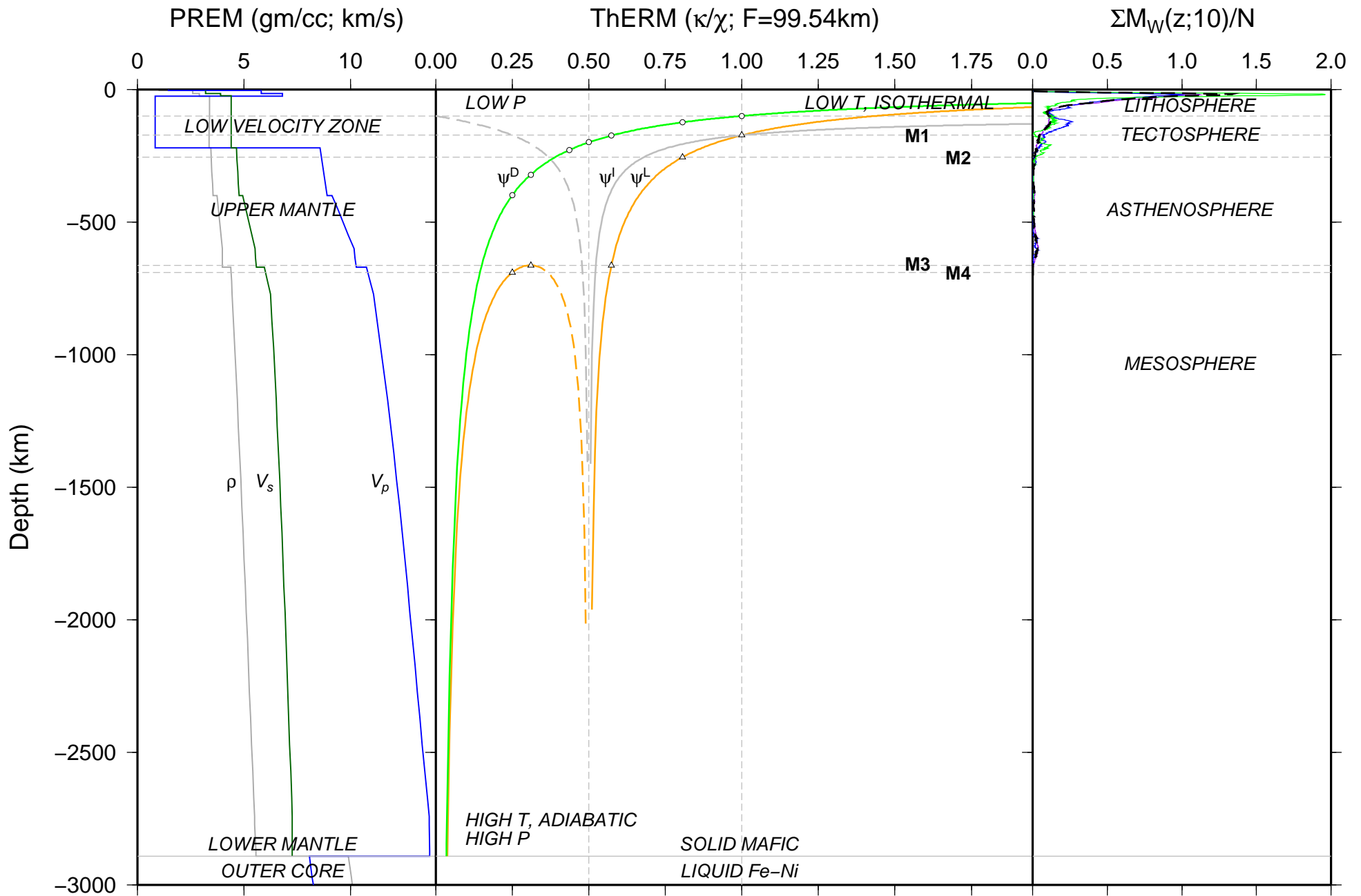
Energy Density ($\Delta U(L)$)

b)



Entropy Density ($|\Delta S(1/L)|$); Radius (R)





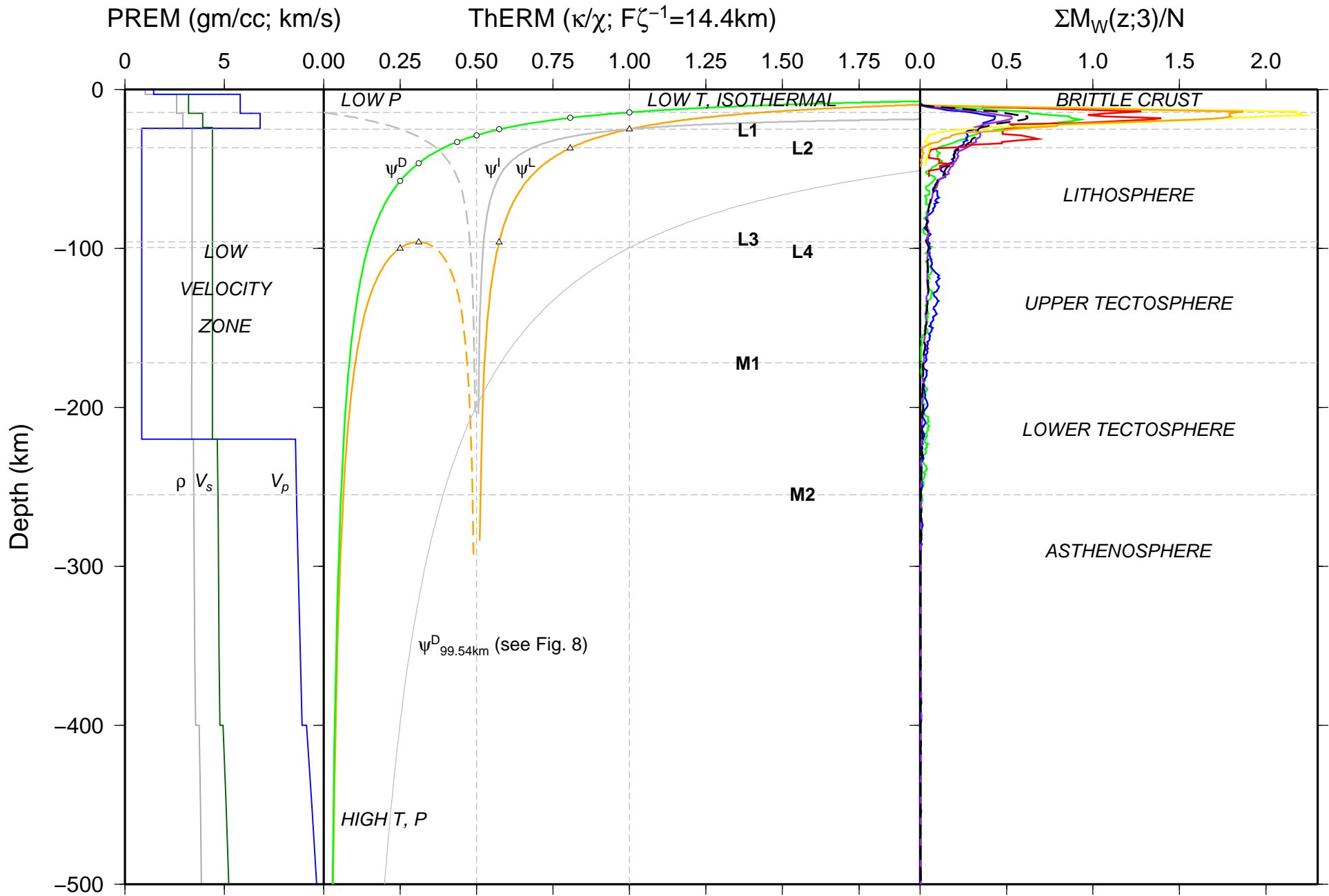


Table 1. Hypocenter and centroid statistics by magnitude

<u>M_w range</u>	<u>Hypocenters</u>	<u>Centroids</u>	<u>Difference</u>
0-1	199	-	(199)
1-2	-	-	-
2-3	-	-	-
3-4	4	-	(4)
4-5	3849	2102	(1747)
5-6	15262	16053	791
6-7	1317	2182	865
7-8	14	292	278
8-9	1	16	15
9-10	-	1	1
Total	20646	20646	0

Table 2. Hypocenter and centroid statistics by depth

<u>Depth range</u>	<u>Hypocenters</u>	<u>Centroids</u>	<u>Difference</u>	<u>Color range</u>
0-14.4	3127	1031	(2096)	red-orange
14.4-25	1051	5268	4217	orange-yellow
25-37	5667	3471	(2196)	yellow-green
37-99.5	5511	5495	(16)	green-blue
99.5-172	2520	2605	85	blue-purple
172-255	941	929	(12)	purple-pink
255-690	1828	1838	10	pink-white
690-800	1	9	8	black
Total	20646	20646	0	

Table 3. Depths to isobaric shears of ThERM (Patton and Watkinson, 2010)

Shear	Depth* (km)	Pressure** (GPa)
H1	3.6	0.10
H2	5.3	0.14
H3	13.8	0.37
H4	14.4	0.39
L1	25	0.67
L2	37	1.04
L3	96	2.96
L4	100	3.00
M1	172	5.40
M2	255	8.27
M3	663	23.4
M4	690	24.5

*F = 99.54 km; $\zeta = 4\sqrt{3}$

**Based on least-squares misfit to PREM (Dziewonski and Anderson, 1981)

Table 4. Centroid-moment magnitude statistics* by tectonic setting

Setting	N	ΣM_w	Max. Z (km)	Plot color
All relocated events	(20646)	(112877)	699	black-dashed
Continental transform	203	1094	47	yellow
Oceanic ridge/transform	1056	5610	49	orange
Continental rift	99	2291	53	red
Himalaya-type convergence	1112	5957	492	green
Island arc-type convergence	15821	86879	699	purple
Andean-type convergence	2511	13887	656	blue
Total (0.8% over sample)	156	2841		

*Correlation coefficient for (N, ΣM_w) population is $r = 0.999899$, with intercept $y = -64.4$

Table 5. Predicted ranges of spherical harmonic degree and frequency for material waves propagating in the boundary layer structure of a thermomechanical Earth

Layer	Depth (km) [*]	Degree ^{**} (<i>l</i>)		Spheroidal [†] (mHz)		Toroidal [‡] (mHz)	
		$\lambda = \zeta d$	$\lambda = 2d$	<i>Low</i>	<i>High</i>	<i>Low</i>	<i>High</i>
L1	25	231	794	25.6	-	23.0	-
L2	37	156	538	15.5	-	15.3	-
L3	96	60	208	6.50	21.0	7.13	23
L4	100	57	200	6.28	20.0	6.93	22.4
M1	172	34	116	4.24	12.0	4.38	13.2
M2	255	22	79	3.08	8.43	3.00	9.20
M3	663	8	29	1.43	3.75	1.35	3.74
M4	690	8	30	1.43	3.85	1.35	4.00

^{*}Isobaric shears of ThERM (Patton and Watkinson, 2009, 2010) with F=99.54 km

^{**}From Jean's relation $l = (2\pi R_{\oplus} / \lambda) - (1/2)$; $R_{\oplus} = 6371km$

[†]Graphical estimates from Figure 8.8 of (Aki and Richards, 2002)

[‡]Graphical estimates from Figure 8.7 of (Aki and Richards, 2002)

Table 6. Experimental results of load-hold tests on Mt. Scott granite (from (Katz and Reches, 2002, 2004)), with estimates of mechanical diffusivity. Sample diameter $d = 25.4 \text{ mm}$.

Sample	l (mm)	τ (min)	Max. NDS	$-\log \chi^*$	Comments
101	66.9	-	1.05	-	load to failure
102	63.5	95	1.03	-	load hold
103	93.8	-	1.02	-	load to failure
104	93.7	61	1.05	5.6	<i>spontaneous failure</i>
105	99.0	180	0.80	-	load hold (1)
→	→	-	1.09	-	load to failure
106	96.1	1.25	1.01	3.9	<i>spontaneous failure</i>
108	100.2	180	0.86	-	load hold
109	98.1	180	0.93	-	load hold
110	94.5	0.03	0.96	2.3	<i>spontaneous failure</i>
112	90.9	-	0.98	-	load to failure
113	96.1	180	0.96	-	load hold
114	96.6	180	0.88	-	load hold
115	93.4	360	0.91	-	load hold
116	97.1	180	0.78	-	load hold
117	89.4	180	0.54	-	load hold
123	95.4	180	0.57	-	load hold
124	76.0	-	0.95	-	load hold (1)
→	→	-	0.96	-	load hold (2)
→	→	-	1.12	-	load to failure
125	83.2	180	0.93	-	load hold (1)
→	→	-	1.05	-	load to failure

*Computed using $\chi = l^2/\tau$